Final Technical Report (ID: DOE-IBM-DE-EE0006334)

Project Title:	Driving CZTS to the SQ Limit: Solving the Open Circuit Voltage Problem
Project Period:	09/30/13 – 10/31/16
Project Budget:	$5,622,071.00
Submission Date:	12/15/2016
Recipient:	IBM T.J. Watson Research Center
Address:	1101 Kitchawan Rd Yorktown, NY 10598
Award Number:	DE-EE0006334
Project Team:	IBM, Univ. of Delaware, Univ. of California San Diego, Harvard
Contacts:	Richard Haight Research Scientist, Principle Investigator Phone: (914) 945-3805 Email: rahaight@us.ibm.com

Glossary:

ALD	Atomic Layer Deposition
CSL	Coincident Site Lattice
CZTS	$Cu_2ZnSn(S,Se)_4$, the kesterite absorber that forms the focus of this project
DFT	Density Functional Theory
DLCP	Drive-Level Capacitance Profiling
DLTS	Deep-Level Transient Spectroscopy
E_G	Band gap
FIB	Focused Ion Beam
FWHM	Full Width at Half Maximum
Fs-UPS	femtosecond ultraviolet photoelectron spectroscopy
GB	Grain Boundary
J-V	Current Density – Voltage
KPFM	Kelvin Probe Force Microscope (x-KPFM is cross-sectional KPFM)
LEEM	Low-Energy Electron Microscopy
MD	Molecular Dynamics
PEEM	Photoemission Electron Microscopy
PL	Photoluminescence
SAD	Selected Area Diffraction
SCM	Scanning Capacitance Microscopy
SEM	Scanning Electron Microscope
SIMS	Secondary Ion Mass Spectroscopy
SQ	Shockley-Queisser (as in Shockley-Queisser limit)
STM	Scanning Tunneling Microscopy (x-STM is cross-sectional STM)
STS	Scanning Tunneling Spectroscopy (x-STS is cross-sectional STS)
TCO	Transparent Conducting Oxide
TEM	Transmission Electron Microscope
TRPL	Time-Resolved Photoluminescence
UHV	Ultra High Vacuum
UPS	Ultraviolet Photoelectron Spectroscopy
V_{oc}	Open-circuit voltage
XPS	X-ray Photoelectron Spectroscopy
XRD	X-ray diffraction

Executive Summary

A key objective of this 3 year research effort was to reduce the open circuit voltage (Voc) deficit, defined as the difference between the absorber band gap and the measured Voc to below 475mV from values at the beginning of this work of 630-730mV. To achieve this reduction, along with the attendant goals of higher Voc and efficiency, detailed studies into the fundamental understanding of existing limitations were undertaken. These efficiency and voltage limiting physical issues include bulk point defects and clusters of defects, electron-hole (e-h) non-radiative recombination at grain boundaries, non-ideal p-n heterojunction formation, back contact problems and the formation of efficiency and voltage robbing secondary phases there and in the bulk. An array of analytical experiments were undertaken and formed the basis of the tasks laid out in the "Statement of Project Objectives". These tasks included:

- Tasks 1, 9, 15 **single crystal growth**. Here bulk single crystals were grown in an effort to isolate bulk defect issues in the absence of grain boundaries. Efficiencies at the beginning of the contract were in the ~1% range but improved to 10% toward the end of the contract. Controlled stoichiometery over the range $0.9< Cu/(Zn+Sn)<1.0$ and $0.9 < Zn/Sn < 1.2$ with single crystal dimensions larger than 2 mm was achieved. Carrier density and mobility targets were achieved and exceeded.
- Tasks 2, 10, 16 **epitaxial film development substitutional cation exchange, AgZTSe** Epitaxial film development was carried out in an effort to avoid the formation of grain boundaries where e-h recombination can occur and to impose long range crystalline structure. Because only limited efficiencies in epitaxial devices were achieved, this work was discontinued in year 2 and converted into Task 10.1 involving bulk defect mitigation through the cation exchange in CZTS,Se, most successfully involving alloying with Ag. 5% efficient devices of AgZTSe were demonstrated and 10%AgCZTSe devices showed 10.2% efficiencies at room temperature and 16.2% at temps below 200K.
- Task 3 **lithographically defined small area device development and large grain devices.** This work was intended to isolate individual grains, fabricate devices at the level of individual grains and establish the role of the grain boundary in limiting efficiency and voltage. Lithographic approaches involved the use of self-assembled microspheres and masking techniques to open micron sized regions. CZTS was then grown epitaxially on the underlying Si. Device measurements on these microcells reached ~345 mV, no better than large area devices and hence this work was terminated after year 1.
- Tasks 4, 11, 17 **surface modification and alternative buffers** This work was undertaken to utilize both ALD and CVD methods to fabricate and deposit new n-type buffer materials to both replace CdS and to offer more robust, tunable buffer materials that could withstand high temperature bakes without decomposition. Buffers including Zn(O,S), $In_2(O,S)_3$, $(In,Ga)_2O_3$ and $(Sn,Ge)O_2$ were explored where in each case the variation in S, Ga or Ge content resulted in changes in band gap and band edge locations relative to CZTS,Se.

- Tasks 6, 12, 13, 18 **material and device characterization** An array of characterization techniques included electrical, optical and electron based approaches. Electrical techniques included standard solar simulator J-V measurements, capacitance studies, temperature dependent J-V, IQE/EQE, Suns Voc, tail states and diode characteristics. Figuring prominently was the invention of an AC Hall probe using master/slave rotating rare earth magnets that created magnetic fields sufficient for Hall utilizing phase sensitive lock-in techniques to measure carrier densities in thin PV absorber films. Further improvements included photo-hall measurements used to extract majority and minority carrier mobilities, recombination lifetimes, minority carrier diffusion lengths. Optical approaches included PL, time resolved PL, temperature dependent PL, PL imaging. Materials characterization included the use of Auger Nano-probe studies of grain surfaces and boundaries with nano-scale resolution and elemental sensitivity, and Kelvin Probe Force Microscopy (KPFM) coupled with grazing angle cryo-Focused Ion Beam (cryoFIB) etching of device layers to extract internal fields of multiple layers. Femtosecond ultraviolet photoelectron spectroscopy (fs-UPS) was utilized to extract band offsets between absorber and buffer, absorber and back contacts and determination of material type (n- or p-) and Fermi level location. In addition to these unique characterization methodologies, SIMS, SEM, TEM, XRD, electron induced x-ray emission for elemental determination were also used.
- Tasks 7, 8, 14, 19 **Density Functional Theory Modeling** Here density functional theory was used to predict key fundamental properties of CZTS,Se, the alloy ACZTSe and the interface between the high work function MoO_3, MoO_2 and CZTS,Se. Key findings were that entropic contributions in the form of Gibbs mixing of constituent elements plus lattice vibrations were key to stabilizing the required Cu poor phase of CZTS,Se at high temperatures. Calculations also showed that cation replacement of Cu with isovalent Ag resulted in a 2x higher barrier to antisite formation resulting in a 10X reduction in defect density. This was observed in a sharpening of the long wavelength spectral edge in EQE and reduction in the gamma parameter. In full AZTSe, the PL peak virtually coincided with the AZTSe band edge indicating very shallow defect levels similar to that observed in CIGSe.

Table of Contents

Background

At present the solar cell industry is growing exponentially in response to the need for renewable energy sources worldwide. The predominant material used for this dramatic increase in utilization is Si, with present module/panel efficiencies nearing 20%[1]. Given the substantial availability of Si in the earth's crust (typically found in its oxidized form) Si based photovoltaic (PV) devices will continue to dominate the industry for large scale use. But Si suffers from two fundamental constraints- it is an indirect gap material requiring the Si absorber thickness to be ~ 300 micrometers (µm) for complete absorption of sunlight and its refinement into an electronic grade single or polycrystalline material is energy intensive. Reduction of Si from SiO_2 can require furnace temperatures in excess of 1500 ˚C to achieve the required purity.

An alternative to bulk PV materials such as Si are the class of thin film PV absorbers fabricated from strongly absorbing, direct gap materials. These materials offer the prospect of substantially thinner (~1-2 µm) devices that typically involve less energy

intensive fabrication. The most successful thin film absorbers for PV are typically multi-elemental compounds or alloys. To date the most efficient multinary, or multi-elemental, thin film PV devices in commercial use today include binary and ternary compounds such as GaAs, CdTe, GaInAs, and more complex compounds such as CIGSe (Cu,In,Ga,Se). III-V based PV devices exhibit the highest single junction efficiencies[2] (~28%) but are extremely expensive to manufacture since they are typically grown on single crystal substrates. CIGSe and CdTe are somewhat less efficient (~22% as of this writing) but far less expensive, and arguably easier, to manufacture. Both of these technologies, though, suffer from limited elemental abundance in the earth's crust (In, Te, Ga), and are mined in relatively small quantities[3]. As an example, examination of the US Geological Survey, (http://minerals.usgs.gov/minerals/pubs/mcs/2015/mcs2015.pdf), shows that only 820 metric tons of In were mined in 2014 (spot price ~$700/kg) compared with more than 26,000 tons of Ag. In and Ga are also subject to substantial competition for use in the electronics industry, eventually limiting scalability of this material for giga- and terawatt power production. An additional disadvantage for CdTe is the toxicity of Cd metal as well as Te, leading to concerns about its widespread use in the environment. Nonetheless solar cells are being manufactured with these materials at the module scale. Another candidate thin film absorber, Pb based organic/inorganic hybrid perovskites have achieved over 20% efficiency[4] but suffers from long term efficiency instability and toxic and water soluble Pb. From an industrial perspective, wide-scale deployment of PV devices for energy generation and for powering autonomous computers and sensors demands stable, non-toxic materials.

To date the most efficient *earth abundant*, *non-toxic* multinary PV devices are fabricated from $Cu_2ZnSn(S_x,Se_{1-x})_4$ CZTS,Se. Despite PV efficiency records of slightly more than half that of both CIGSe and CdTe, this photovoltaic absorber may eventually achieve improved performance through additional alloying and/or novel device architectures to compete with other technologies. Alloying with Ag is described in Tasks 10.1 and 16. Detailed studies of the defects in this material have shed new light on potential paths for improvement and are discussed in Tasks 7,8,14,19. Some of these approaches include modification of the back contact of CZTS,Se based devices (Tasks 6,12,18) and substitutional alloying with Ag in an effort to address bulk point defect limitations. From its low efficiency beginnings[5][6] to its present day peak of 12.6%[7] our work has illuminated fundamental understanding of factors that limit increases in efficiency, due in great part to bulk point defects, primarily Cu/Zn antisite defects and clusters of defects. A combination of electrical, optical and electronic characterization is coupled with device simulations and ab-initio calculations to identify the fundamental bulk properties and performance limitations associated with these defects were carried out. Our detailed studies of grain boundaries led to our discovery that these surfaces were terminated with tin oxides that formed following air anneal resulting in increased device performance.

We have studied in detail the p-n heterojunction and the determined the valence and conduction band offsets measured with femtosecond ultraviolet photoelectron spectroscopy (fs-UPS) coupled with optical spectroscopies. We have also carried out back contact engineering experiments involving exfoliation of full devices that reveal the back absorber surface and our recent experiments designed to study and engineer the back contact to increase open circuit voltage, Voc. We carried out unique experiments on

cation exchange involving alloying CZTS,Se with Ag that inhibits anti-site defect formation[8]. Ag-alloying has led to high device efficiencies and shows substantial promise for achieving even further efficiency increases through process optimization. As an example we have achieved a low temperature (<200K) efficiency of 16.2% for the alloy $Ag_{0.1}$ $Cu_{0.9}$ ZTSe, which stands as the highest efficiency achieved to date, at any temperature, in the earth abundant kesterites and suggests the possibility of eventual increases in efficiency beyond 12.6% at room temperature. In addition to devices alloyed with Ag, pure AgZTSe devices have been fabricated, with efficiencies in excess of 5% [9].

Introduction

As described in the Background Section above, work under this contract has been devoted to identifying the basic issues that limit increases in open circuit voltage and overall efficiency of CZTS,Se and to utilize that knowledge to achieve improvements. Efforts to attack these problems included

1. growing macroscopic single crystals of several mm in size and greater to isolate bulk issues in the absence of grain boundaries
2. epitaxial growth to address atomic organization in the crystals and produce crystalline thin films without grain boundaries
3. lithographically delineated small regions of polycrystalline thin films in an attempt to isolate individual grains and to fabricate ultrasmall devices in an effort to compare device performance at the single grain level with macroscopic multi-grain devices
4. cation substitution to attempt to correct Cu/Zn antisite defect formation that occurs when Cu and Zn, whose covalent radii are nearly identical and whose formation results in a continuum of states within the band gap called band tailing that leads to reduction in device voltage
5. highly controlled buffer deposition via atomic layer deposition (ALD) and chemical vapor deposition (CVD) utilizing robust materials with large band gaps that, via elemental concentration changes can optimize band edge alignment
6. detailed characterization techniques that used a wide array of electrical (J-V, Suns Voc, T dependent CV, Hall and Photohall measurements of both majority and minority carriers, TEM, SEM, EDX, XRD, T dependent photoluminescence, fs-UPS to measure band bending, Fermi level location and band offsets, KPFM to measure work function differences and fields and Nano-Auger to study elemental distributions at surfaces and grain boundaries with nanoscale resolution
7. exfoliation experiments that removed the back Mo/glass contact, revealing the back surface of CZTS,Se devices and permitting the treatment (e.g. etching, film deposition) and deposition of a high work function/reflective back contact to increase Voc, current and overall performance
8. density functional calculations to identify and study the key bulk defects that limit Voc, to determine whether cation substitution such as Ag alloying or full

replacement of Cu reduces or eliminates the generation of bulk defects. It was shown that entropic contributions of Gibbs mixing of Zn and Sn as well as lattice vibrations led to increased phase space availability for the formation of CZTS,Se. DFT calculations of MoO_3 and MoO_2 interfaces with CZTS,Se showed the importance of oxidation in the formation of these interfaces. DFT calculations were critical throughout the contract.

In (1) considerable success was achieved in increasing single macroscopic crystal efficiencies and Voc from ~1% to ~10% at the end of the contract by optimizing growth processing, polishing and surface passivation.

In (2) epitaxial growth was successfully achieved but extremely high carrier densities in the range of $10^{19}/cm^3$ led to shunted devices- these problems were insurmountable and this activity was terminated (no-go) in year 2.

In (3), it was found that lithographically isolated regions produced sub-par device performance and this work was also terminated (no-go) in year 2.

In (4) cation substitution and alloying of Ag with Cu was used to reduce the density of point defects in the thin film absorber and led to improvements in performance particularly as we achieved 16.2% efficiency for alloyed AgCZTSe below 200K and also reported spectroscopic results that showed significant decrease in band tailing in both alloyed and pure Ag devices. This work was initiated in year 2 and continued to the end of the contract.

In (5) an array of wide band gap buffer materials were successfully deposited and this work was carried out throughout the contract. Although use of these buffers did not lead to higher efficiencies than were achievable from chemical bath deposition of CdS, they did usher in a new class of band gap tunable, robust buffer candidates. Particularly when AZTSe, a new PV material was found to be n-type, work on CuBr, Cu_2O and CuI was carried out to provide a new class of p-type buffers for use with AZTSe.

In (6) characterization modalities were indispensable in identifying key problems and pointing to solutions. For example Auger nanoprobe work conclusively showed that air anneals of CZTS,Se led to the formation of passivating tin oxides at the grain boundaries that dramatically reduced electron-hole nonradiative recombination there. Fs-UPS studies showed which buffers led to beneficial band lineups with CZTS,Se, upward band bending at the CZTS,Se/MoO_3 interface indicating that a beneficial electrostatic field was established leading to higher Voc's, KPFM confirming this with measurements of work functions of buried interfaces, and the wide range of electrical characterization and PL studies that revealed electron and hole carrier densities and mobilities, a new 16.2% efficiency albeit at temperatures below 200K in alloyed AgCZTSe and indications as to what passivation treatments of both front and back CZTS,Se surface led to higher Pl and efficiencies.

In (7) exfoliation experiments were initiated in year 2 and continued to the end of the contract. These experiments definitively showed that we could modify the electrostatic field at the back of the contact by deposition of a high work function MoO_3 material followed by a reflective cap of Au that resulted in increasing Voc with reduced CZTS,Se absorber thickness. In addition we discovered that even on thick absorber substrates of 2 microns, that exfoliation and deposition of MoO_3 and Au produced improved results.

The use of ammonium hydroxide or KCN to remove secondary phases that occur at the back of the device along with the new back contact produced higher fill factors and increased Jsc as well as increases (though modest for the thicker films of 5-7mV) in Voc. This work led to the development of series connected monolithic devices that for 9 cells could produce voltages as high as 5.7V.

In (8) density functional theory (DFT) was used as described above to study point and clusters of defects, the reduction in defect density with cation (Ag) introduction and interfaces between CZTS,Se and Mo oxide layers.

Project Results and Discussion

Tasks 1, 9, 15: Single Crystal Growth: Brian McCandless, University of Delaware

Our goal was to use single crystals as a model system to better understand the challenging defects in $Cu_2ZnSnSe_4$ absorber layers for solar cells. It was necessary to develop new methods to fabricate single crystals, measure defect properties, and develop solar cells. The 1-dimensional device architecture facilitated exploration of bulk and surface recombination effects on device performance using SCAPS simulation. Both bulk and surface defects for single crystals and films were investigated with photoluminescence methods and manipulated to reduce recombination and improve V_{OC}. For the surface that becomes the electrically active junction, new passivation methods were developed. For the bulk, variations in stoichiometry, dopants, and temperature equilibria were explored. Bulk incorporation of the critical dopant Na was measured for the first time and the effects on sub-Eg states were demonstrated. Further manipulation of defect populations by temperature equilibria are shown to change sub-Eg defects critical for band-tailing. Single crystal devices were demonstrated for the first time. Using optimized methods for improving surface and bulk defects, a single crystal device of 10% efficiency was demonstrated with a voltage deficit equal to record thin film devices, V_{def} = 530 mV. Devices with a deposited passivation layer yielded V_{def} < 400 mV, demonstrating that the junction interface exerts the dominant control over the V_{OC} for crystal with sufficient bulk electron lifetime, τ_e >1 ns.

Significant Accomplishments

1) Gradient freeze method adapted for crystal growth developed without flux agent;
2) New fundamental data obtained showing effect of stoichiometry on carrier concentration, hole density of states, and lifetime: low Cu yields low p-conductivity and high PL intensity, hole DOS ~3E18 cm^{-3};
3) Limits of equilibrium phase diagram suggest thin films in pseudo-equilibrium growth regime, can achieve wider phase space;
4) High-angle x-ray diffraction confirmed phase, Laue diffraction confirmed monocrystal;
5) Chemical treatments developed which significantly improve surface passivation;
6) Temperature equilibria and quench vs slow cool reveal the limits of ordering and band tailing based on equilibrium system having less surface, no grain boundaries;
7) Na diffusion quantified in-terms of solubility and rate at intermediate processing temperature (420C), paired with Talia Na defect study shows Na passivation;

8) Employed SCAPS device simulations to guide device development, from low efficiency and voltage to improved surface preparation, and subsequent record efficiency and V_{OC} deficit;
9) New device architecture with tailored interface yields record low V_{OC} deficit, <400 mV.

Crystal Growth

Bulk p-type single crystals of $Cu_2ZnSnSe_4$ (CZTSe) and alloys thereof, with multi-millimeter dimensions, were grown for solar cell absorber layers to discover pathways for reducing the open circuit voltage deficit in *thin-film* solar cells. A bulk single crystal approach was identified to unambiguously separate effects of bulk crystal properties from surface and interface condition. Single crystals, by definition, are grain boundary-free and allow access to multiple re-processing cycles. To further reduce the complexity of the solar cell problem, crystals with selenium-based anion composition were grown, without fluxing agents, dopants, or other intentional impurities. The independent variables employed over the course of the project were: Cu/(Zn+Sn) composition; elemental versus compound precursors (ZnSe + Cu_2SnSe_3); maximum temperature reached during growth; temperature-time profile growth profile; and post-growth cooling rate. Three furnaces were configured to provide the necessary temperature and time control, and 53 separate runs, each consisting of two to four 1-1.5 cm diameter ampoules with 10-20 g of total charge each, were made – each ampoule yielded 5-10 large crystals, generating an inventory of several hundred crystals. Selective screening crystals by size (>3 mm), composition (0.8<Cu/(Zn+Sn)<0.95), and resistivity (>1 Ohm-cm) produced a set of about a hundred crystals from which devices were fabricated.

At the beginning of the project, the team was aware of only one group making significant progress in growing kesterite boules using excess tin as a fluxing agent [10][11]. To prevent the pinning of the single-phase region on the Sn-Se phase boundary with a Sn flux, and avoid contamination from molten salts, we focused mainly on a high-purity crystal growth mechanism involving no excess elements. The IEC crystal growth evolved over the project from the “travelling heater method” with short processing times (~1 week) and yielding non-uniform boules with 1 mm crystals, to an improved approach called “gradient freezing”, with the ampoule spanning a fixed temperature gradient at maximum temperature *below* the quaternary decomposition temperature, <800°C, enabling growth of dense individual well-faceted grains in the specified composition space but requiring more time to obtain facets exceeding 2 mm (see Figure 1, left). By the end of the project, crystals approaching 5 mm size were obtained in $Cu_2ZnSnSe_4$, $(Ag,Cu)_2ZnSnSe_4$, $Cu_2(Zn,Mn)SnSe_4$, and $Cu_2ZnSn(S,Se)_4$ compounds. Ancillary experiments were conducted to use a flux agent (sodium selenite) to decrease processing time, but this increased wall adhesion more than facet size. Also, rapid thermal heating of kesterite powder at 1 atmosphere in argon at ~780°C to sinter it without loss of volatile $SnSe_2$ did yield sintered material but did not produce gross grain growth.

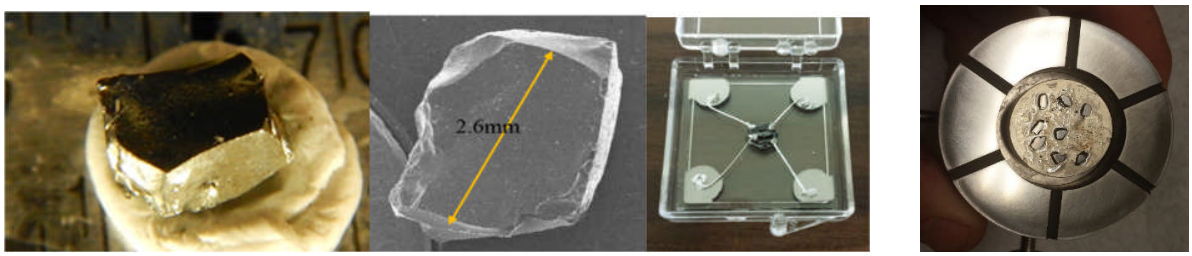

Figure 1. $Cu_2ZnSnSe_4$ crystals fabricated during the first quarter: White light and SEM image of extracted crystals (left); crystal mounted for Van der Pauw resistivity and Hall measurements (center); and 8 crystals mounted on polishing platen (right).

Bulk Properties

The targeted compositions ranged from stoichiometric to Cu-poor and Zn-rich as empirically found for high performance thin film devices, with Cu/(Zn+Sn) from 0.8-1.0 and Zn/Sn from 1.0-1.2. The firing of elements in a single "run" is called direct synthesis, and re-firing of these materials in a larger diameter ampoule is called compaction. Three cooling methods were employed: very slow (1°C/hr), slow cooling (100°C/hr), and quench cooling (100°C/sec). Figure 2 shows that boules quenched from above the quaternary melt are phase segregated along the boule length. Quench-cooling from temperatures below the melt produced a thicker band of the quaternary. Refinement of growth relied on an intermediate hold temperature during the early stage to use the ternary melt as a flux agent. Quenching from different hold temperatures generated crystals with different disorder.

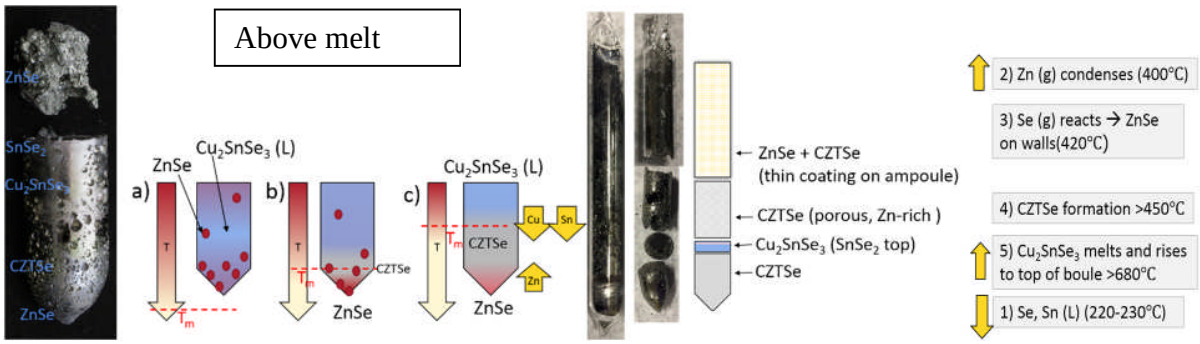

Figure 2. Conceptual reaction model of vertical boule growth above and below melt from quenched ampoules during ramp and growth stages.

X-ray powder diffraction (Figure 3) and Laue diffraction (Figure 4) verified the single-phase composition and single crystal nature of the crystals extracted from the boules. Powders prepared from extracted crystals exhibited high-angle diffraction peak patterns that match calculated intensity patterns for the I-4 space group with random Cu-Zn ordering; the use of high-angle peaks removes the ambiguity of phase overlaps introduced by ZnSe and Cu_2SnSe_3. Digital Laue images showed sharp distinct patterns consistent with the tetragonal unit cell, with rotational validation. The naturally occurring faces exhibited mirror and two-fold symmetry, with some faces indexed as [110].

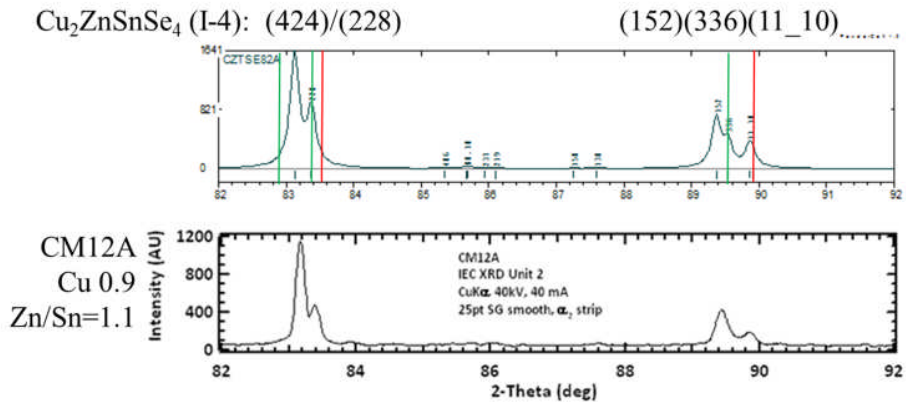

Figure 3. High 2θ x-ray powder diffraction patterns: calculated for Kesterite (I-4) structure (top) and measured for polycrystalline sample (bottom) taken from compaction ampoule CM12 (bottom). Superimposed on the calculated pattern, red and green lines indicate positions of ZnSe and Cu_2SnSe_3 reflections, respectively.

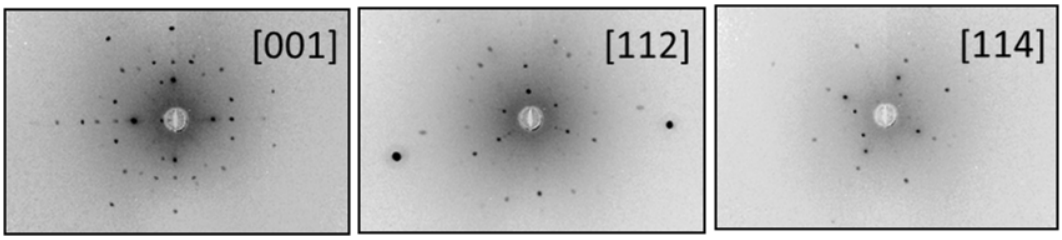

Figure 4. Laue images of 4 mm single crystal of $(Ag,Cu)_2ZnSnSe_4$ after rotation of [001], [112], and [114] crystal axes with incident beam.

Lattice refinement of XRD patterns of powders from different synthesis methods revealed two phenomena: 1) slow-cooled (3°C/hr) showed lattice compression, with c/a = 1.991 and 2) intensity patterns change over time with powder air exposure, which has strong implications for CZTSe surfaces.

We further explored the cooling-disorder relationship via photoluminescence spectrum measurements. Figure 5 shows the PL spectral peaks/shapes for a quenched (500°C) crystal and a slow cooled crystal (3°C/hr to 25°C). We observe a peak shift to higher energies with the slow cooling treatment that has been noted previously in literature [12]. Interestingly, evidence of disorder was more prevalent in the slow-cooled crystal. The blue shift with excitation intensity which is expected for disordered materials [13] was observed to be nearly 5x as large in this sample. Furthermore, the width of these peaks are larger than for the quenched sample, a further indication of increased disorder. These observations provide evidence that defect clustering may be occurring with the slow-cooling treatment. This suggestion is further supported by the results provided by UCSD indicate that antisite defect formation energy lowers in the presence of other similar defects [14].

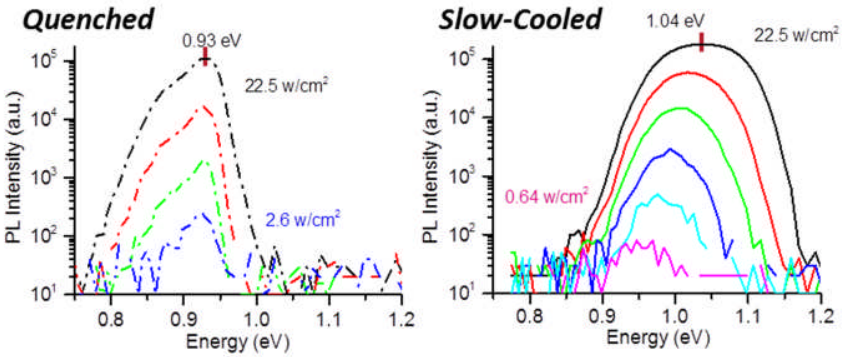

Figure 5. PL intensity spectra of quench-cooled and slow-cooled CZTSe crystals.

Electronic properties were routinely measured on selected samples from each group of crystals, yielding crystal resistivity, majority carrier type and concentration, hole mobility, bulk lifetime and surface recombination velocity. Figure 6 [left] shows that for pure $Cu_2ZnSnSe_4$, the hole concentration (p) drops exponentially with decreasing Cu content (blue diamonds). Alloys with silver (red circles) or sulfur (black squares) exhibit a similar trend but with lower carrier density. The implication for devices is that excessive hole concentration will result in a very narrow space-charge region, subjecting the junction to high fields and surface defects, and forcing the device into a diffusion collection regime. So solar cells were fabricated on crystals with p = E15-E17 cm^{-3}. The Seebeck coefficient versus log (p) shows a tight trend for all the samples, consistent with a hole density of states of 3E19 cm^{-3}, which is similar to first-principles values [15] and is necessary for device simulations. Hall-measured hole concentrations were consistent with charge density measured by capacitance-voltage in solar cell devices. Hole mobility ranged from 50 to 150 cm^2/V-s with no composition or temperature-time profile trends. Electron lifetime measured by TRPL typically yielded values of τ_e~1.5 ns, and one crystal measured by terahertz spectroscopy exhibited τ_e~10 ns.

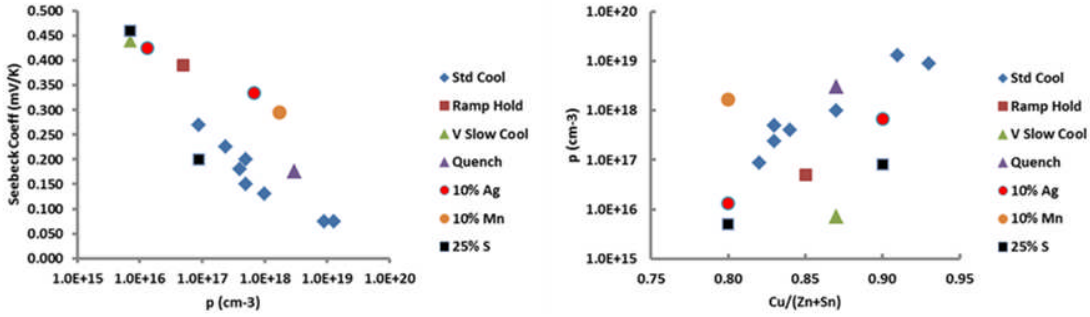

Figure 6. Resistivity versus Cu/(Zn+Sn) [left] and Seebeck coefficient versus resistivity [right] for representative samples from different processing groups.

A procedure was developed to mechanically reduce crystal thickness to ~60 microns, where direct absorption measurements become possible in conventional NIR spectrophotometer. One sample was subjected to this lengthy process and yielded a

linear α^2 vs E absorption curve, with extrapolated band gap of 0.98 eV, which is consistent with the band edge found in our device EQE long wavelength fall-off.

In thin film CZT(S,Se) solar cells, as with CIGSe-based solar cells, sodium playes a role in controlling conductivity and grain boundary passivation. We investigated both bulk and surface effects of sodium. In one case, NaF was evaporated onto a polished CZTSe crystal surface and heated at 420°C for 6 hour. SIMS depth profile analysis showed a rapid decline in F signal but a deep Na diffusion tail, yielding a near-surface solubility ~4E17 cm^{-3} and bulk diffusion coefficient of 2E-11cm^2/sec. Halide salt treatments of surfaces were also investigated as passivation agents using PLI (below).

Surface Properties and Passivation

Microscopic analysis and Raman spectroscopic analysis show the crystal surfaces can contain $SnSe_2$ and Cu_2SnSe_3. This mandated the need for surface preparation prior to device fabrication. Photoluminescence imaging (PLI) was developed as a tool to evaluate the quality of single crystal surfaces. The technique was applied to different surface treatment techniques including solution etching, annealing and passivation layers (ZnSe). Figure 7 [left] highlights the improvements in PLI signal that accompanies Br-MeOH solution etching as a function of treatment time and crystal composition. The improvement in PLI intensity was shown to correspond with improved device performance, indicating a passivation of the interface defect layer (IDL). A decrease in PLI was also noted over time for as-etched surfaces, indicating that other factors than IDL passivation were effecting the overall surface quality. The effects of annealing in a laboratory atmosphere on PLI is also highlighted in Figure 7 [right]. These results provide evidence that surface improvements are the dominant mechanism behind device improvements that have been observed with anneals at 350˚C demonstrated by both the IBM and IEC collaborations. Other PLI enhancements were found using 100 nm thick coatings of group I halides, such as LiF, NaF, and KCl, followed by air annealing. Finally, a transient reflection measurement of a Br-etched bare CZTSe surface yielded a surface recombination velocity = 8700 cm/s.

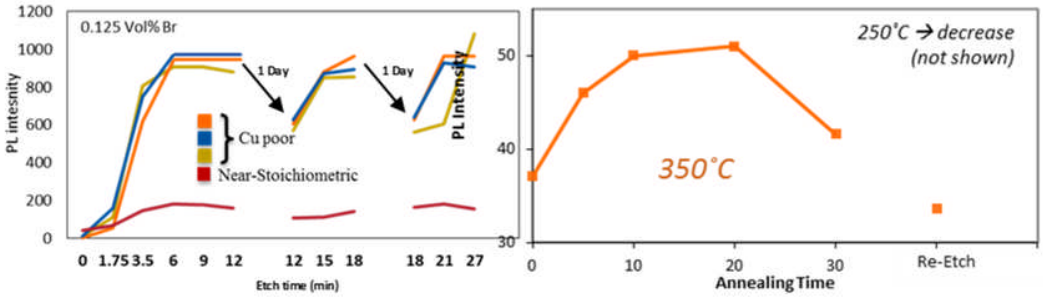

Figure 7. [Left] PL intensity versus sequential etch showing two cycles of degradation over 7 days in ambient, followed by re-etching. [Right] PLI dependence on air annealing time at 350°C; anneals at 250°C were not beneficial.

Solar Cell Development

The basic cell design derived from the CIGSe/CdS thin film solar cell. However, CZTSe solar cell fabrication involved additional steps to either establish a bulk property or modify

a surface. Figure 8 is a comparison of the “best” approaches found for CZTSe films and single crystals, with the important distinction being that the crystal is damaged after growth, during the removal of surface phases and planarization. The damage is repaired by grinding the surface with progressively finer abrasives, followed by a chemo-mechanical polish (CMP) which we developed based on “figure-8” motion on a soft carrier, saturated with weak bromine-methanol. Both types of cells receive an air anneal, which the IBM and UCSD team members have shown produces an oxide surface that is reduced by the CdS CBD bath.

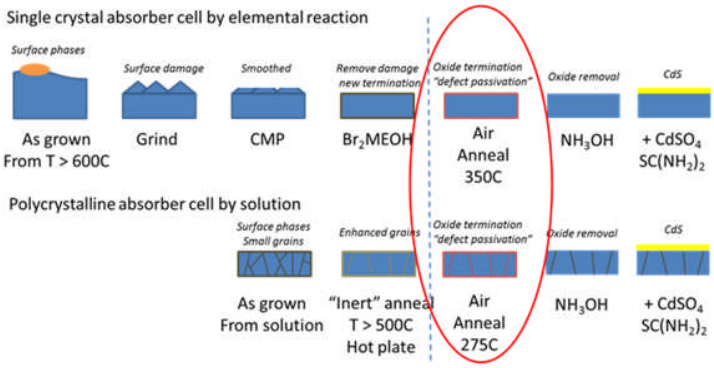

Figure 8. Cell fabrication sequence for crystal cells [top] and films [bottom].

Our early devices exhibited V_{OC} < 100 mV and efficiency <1% because we employed crystals that were too conductive and had highly damaged surfaces. By the end of the first year of the project, however, we demonstrated cells in the 5% efficiency range. To move ahead we needed to understand the relative influence of bulk and junction interface properties on device performance, we relied on SCAPS, version 3.3.02, with input values we either measured or identified from literature. Our earliest devices had V_{OC}~200 mV and exhibit poor photocollection but with the collection edge at 0.95 eV. We were only able to simulate those early JV curves by introducing an interface defect layer (IDL) into the model. The origin of this layer was linked to the mechanical abrasion process used to planarize the sample, plus reaction of the exposed surface after etching with ambient. The simulations indicated that the greatest gain in Voc was obtainable by eliminating the IDL, suggesting V_{OC} deficits <470 mV were feasible. Increasing bulk electron lifetime by 100X primarily influences the photocollection, necessary for high efficiency.

Over the course of the project, cell fabrication was an iterative process, often involving re-use of a crystal that previous showed a promising device result, coupled with a newly refined processing step. In each device-fabrication group, so-called ‘champion cells’ tended to originate from specific ampoules, meaning specific crystal growth procedures, such as SY14, CM14, SY24, SY43, which were grown below the quaternary decomposition temperature. Given this, the best device performance was governed by the quality of the passivation prior to CdS deposition, based on PLI results. The lowest V_{OC} deficits (qV_{def}) we obtained are listed below for E = 0.95 eV.

Passivation	Voc (mV)	qV_{def} (meV)
Br only	420	530
50 nm ZnSe	390	560

10 nm ZnSe	390	560
100 nm CIGSe	590	360
10 nm CIGSe	490	460

Tasks 2, 10: Epitaxial Film Development, Talia Gershon, IBM

The CZTS a-axis lattice constant has a near perfect match to that of Si, at ~ 0.543 nm. In our first year, we established epitaxial growth conditions for preparing CZTS (pure sulfide) films on Si substrates of both (100) and (111) orientations. Selected-area diffraction patterns (SADP's) were recorded in accordance with our SOPO milestones, and these further confirmed the epitaxial relationship (Fig. 8a-d). Also in line with our SOPO targets, the grain size of our material was over 10 microns (Fig. 8e), the ratio of epitaxial to non-epitaxial peaks in our material's x-ray diffraction (XRD) pattern was over 50, and the full-width at half-maximum (FWHM) of the XRD rocking curve was 0.5º. An HF dip of the substrate prior to growth, to remove the native silicon oxide, was found to be an important preparation step. Additionally, samples grown at 370ºC were found to have a high density of twin boundaries, whereas these structural defects were not observed in samples grown at 450ºC.

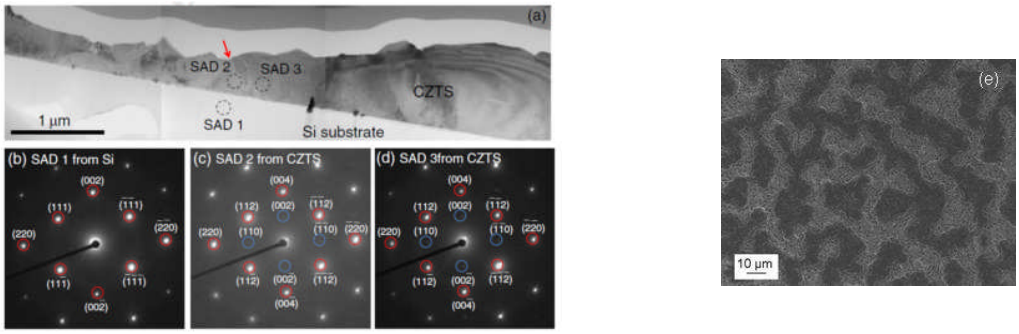

Figure 8: (a) Bright-field TEM image of an epitaxial CZTS sample on silicon (100) showing a typical grain (three images taken from areas next to each other were stitched together). The dotted circles indicate where the SADP's shown in (b-d) were taken. (b) SADP from Si substrate, (c-d) two different regions of CZTS. Images (a-d) were reproduced from Ref. [1]. (e) Top-down SEM image of epitaxial CZTS on Si (100), showing that grains larger than 10 microns have been achieved.

We dramatically improved the epitaxial thin film microstructure by working with CZTSe instead of CZTS. We made this change because of our finding that sulfur etches silicon and prevents uniform film growth. This can be seen in Figure 9a and 9b, which show pitting in a masked region of the Si substrate after a typical CZTS deposition. Consequently, the CZTS microstructure was poor (Figure 9c). By switching to CZTSe, we prohibited wafer etching and achieved uniform thin films on both Si (100) and (111) (Figure 9d,e respectively). Improving the uniformity of the substrate also improved the epitaxial relationship between CZTSe and the silicon (not shown), despite the fact that CZTSe has a larger lattice mismatch with Si (4%). The FWHM of the XRD rocking curve was reduced to a minimum value of 0.35°. The improved film microstructure allowed us to measure the electrical properties of our epitaxial CZTSe by using an exfoliation technique developed at IBM by Dr. Oki Gunawan. The carrier density was measured to be 1.1 x 10^{19} cm^{-3}, with a mobility of 0.59 $cm^2V^{-1}s^{-1}$. Although this carrier density value

was too high for efficient device operation, the mobility value was higher than that of our best polycrystalline CZTSe material (0.47-0.51 $cm^2V^{-1}s^{-1}$). This high carrier concentration, however, resulted in shunted devices.

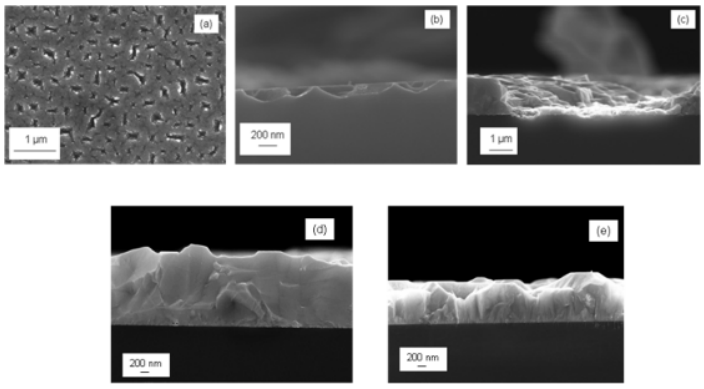

Figure 9: (a, b) Top-down and cross-sectional SEM images (respectively) showing pitting in the silicon wafer due to sulfur etching. (c) Cross-section of an epitacxial CZTS film on silicon showing poor film coverage where etching has occured. (d,e) Cross-sections of CZTSe samples grown on Si (100) and Si (111), respectively. The same etching of the underlying silicon substrate is not observed.

Unfortunately, all epitaxial CZTS(e) samples prepared in this project had poor photoluminescence efficiencies and short minority carrier lifetimes, likely due to the high carrier concentration and/or the presence of additional non-radiative recombination centers within the film bulk. None of the epitaxial CZTS(e) materials were competitive with the polycrystalline thin films with regard to device performance. In parallel, detailed photoluminescence experiments were conducted to determine the extent to try to quantify the differences between the bulk properties of CZTS(e) and CIGS, to understand the bulk contribution to the performance losses[16]. It was found that CZTSSe suffers from (1) deeper defect states relative to the band edges, (2) a larger degree of band tailing, and (3) a higher density states that cause non-radiative recombination. For all of these reasons, the research focus shifted to another type of "model system", namely substitutional alloying, which was believed to offer a potential solution to the bulk problems which give rise to the V_{oc} deficit in CZTSSe (described in Task 16).

Tasks 10.1, 16: Bulk defect mitigation via substitutional cation exchange into CZTS(e), Talia Gershon, IBM

With the help of the UCSD theory team, we learned that replacing some or all of the Cu in CZTSSe with Ag was a promising approach for reducing the density of bulk antisite defects and consequently improving the Voc. This is because Ag-Zn antisites have a higher formation energy than Cu-Zn antisites, and therefore these defects should form less readily[14][17] Therefore, we completed and published a detailed study of the impact of Ag alloying on the fundamental optical and electronic properties of $(Ag,Cu)_2ZnSnSe_4$ (ACZTSe)[18]. We demonstrated a technique for controllably tuning the Ag:Cu ratio and documented the impact that this has on the carrier concentration, extent of band tailing, and extent of Fermi level pinning. Figure 10 shows that we observe the predicted

structural changes in ACZTSe with Ag alloying, and consequently a shift in the main (112) diffraction peak towards lower 2theta (Fig. 10a) due to the larger lattice constant (Fig. 10b). Thus, we showed that Ag is readily alloyed into CZTSe resulting in the desired structural properties, thereby satisfying a key SOPO requirement.

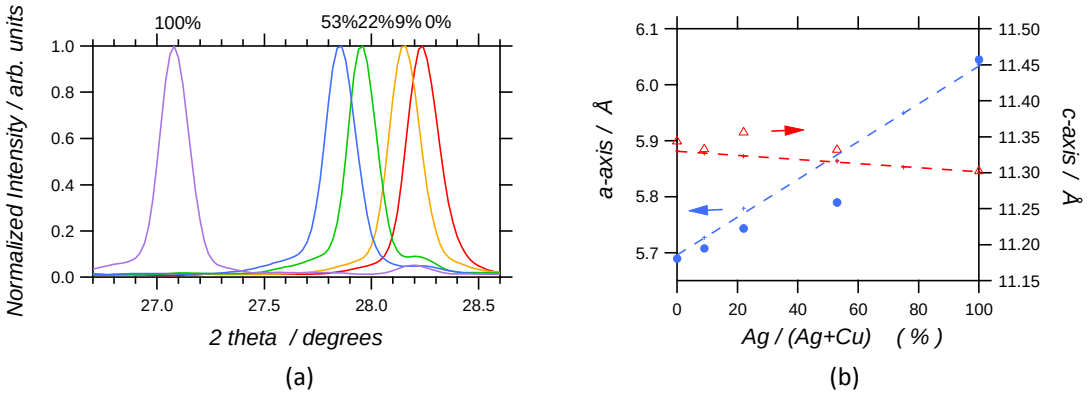

Figure10: (a) Shift in the position of the main (112) diffraction peak of ACZTSe as a function of Ag concentration in the absorber due to (b) the change in the lattice constant of the material with increasing Ag concentration. From Ref. [18]

Figure 11 shows the impact of this alloying on the optical properties of ACZTSe (another SOPO requirement). In Fig. 11a, the top portion of the graph shows the Tauc plots, created from UV-VIS transmission data, to extrapolate the optical band gap of the materials. The lower portion of the graph shows room-temperature photoluminescence data from the same samples. In the case of low-Ag, we observe photoluminescence at significantly lower energies (~ 100 meV) than the band gap energy, which indicates that electron-hole pairs relax into deep states in the band tails prior to radiative recombination. This difference between the band gap energy and the peak photoluminescence energy has been correlated with the extent of band tailing in CZTSSe as well as the observed Voc deficit[19][20]. In Fig. 11b is can be seen that Ag alloying significantly suppresses band tailing even for low-to-moderate Ag concentrations (<50%), and thus should enable significant improvements in the Voc of CZTSSe devices. This result achieved an important SOPO milestone. Initial experiments already reveal a Voc-deficit reduction of ~ 40-60 mV for samples containing only 10% Ag[18] thereby reaching the SOPO go/no-go decision. However, with 10% Ag alloying we also observe a carrier density too high for optimum device performance (Fig. 12a) which points to an area for improvement.

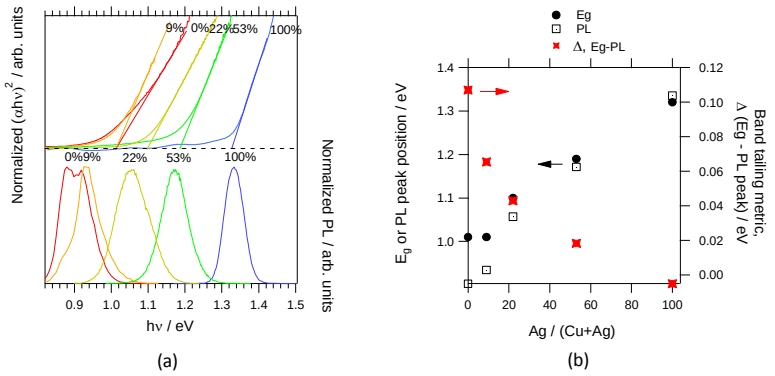

Figure 11: (a) Comparison of band gap energy (top), extrapolated from Tauc plots created using UV-VIS transmission data, with the peak photoluminescence energy (bottom). The difference between these energies is considered to be indicative of the extent of band tailing in the absorber. This energetic difference is plotted in red in (b).

Ag-alloying also has an impact on the electronic properties of ACZTSe thin films (a SOPO requirement). Figure 12 summarizes the impact on carrier concentration (Fig. 12a), majority carrier mobility (Fig. 12b), and Fermi level position (Fig. 12c). The pure-Cu CZTSe material is intrinsically p-type with a carrier density of ~ 10^{16} cm^{-3}; in contrast the pure-Ag AZTSe is intrinsically n-type with a much lower carrier density of ~ 10^{11} cm^{-3} (Fig. 12a) This difference is due to a change in the types of native defects that are most energetically favorable to form and ionize in the materials. Intermediate Ag concentrations display majority carrier concentration and types in between those of the pure-Cu and pure-Ag compounds, as could be expected. Similarly, as Ag is increasingly alloyed into CZTSe, an increase in majority carrier mobility is observed (Fig. 12b). For the full-Ag compound, the mobility has been measured to be as high as ~ 100 cm^2/Vs, although the inversion to n-type may also help explain this observation, since it is common for the electron mobility to exceed that of the hole mobility in most materials due to the difference in band structure geometries. Importantly, the Fermi level is found to un-pin from mid-gap at high Ag concentrations (Fig. 12c). In CZTSe, despite having a high hole density of (10^{16} cm^{-3}), the Fermi level is frequently found mid-gap due to severe band tails (in contrast, classical semiconductor theory predicts 0.1 eV from the valence edge for this doping level). The mid-gap Fermi level location in CZTSe has been attributed to the role of defect compensation and band tailing. In contrast, the Fermi level of AZTSe is found to be 0.3 eV from the conduction band edge, which is equal to the prediction of classical semiconductor theory based on the carrier density measured by Hall; this is further evidence of a significant suppression of the band tailing, which is considered to be the primary cause of Voc loss in CZTSSe photovoltaics.

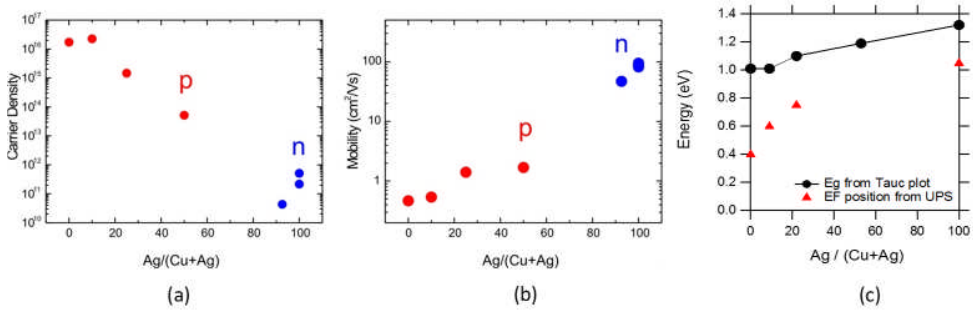

Figure 12: (a) Carrier density, (b) majority carrier mobility, and (c) Fermi level position relative to the valence band edge for ACZTSe materials across the range of pure-Cu to pure-Ag.

We have also prepared an AZTSe-based photovoltaic device with ~5% conversion efficiency using a Schottky-type architecture with a MoO_3 buffer and a SnO_2:F (FTO) bottom electrode (Figure 13).[9] This electrode was selected on the basis that it forms an Ohmic contact to AZTSe, whereas Mo does not (due to the formation of a high-work function $MoSe_2$ layer). We then completed a comprehensive study of the impact of composition of AZTSe on the grain structure, conversion efficiency, and optoelectronic properties, which is summarized in Figure 14. We found that large grains in AZTSe were achieved with the highest Ag content in the absorber, indicating that excess Ag may act

as a flux agent during growth. We also found that Ag-poor compositions reduce the performance of AZTSe-based devices, and achieving a composition close to stoichiometry is important for the best efficiency. These results are discussed in great detail in a manuscript, which has been submitted for publication.[21]

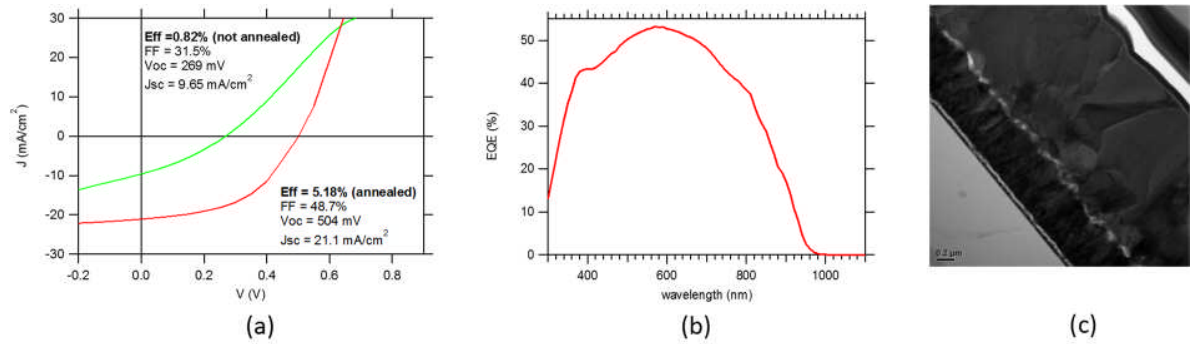

Figure 13: (a) J-V curves showing that efficiencies over 5% have been achieved using an AZTSe buffer. (b) EQE data from this sample, (c) cross-sectional TEM image of the absorber.

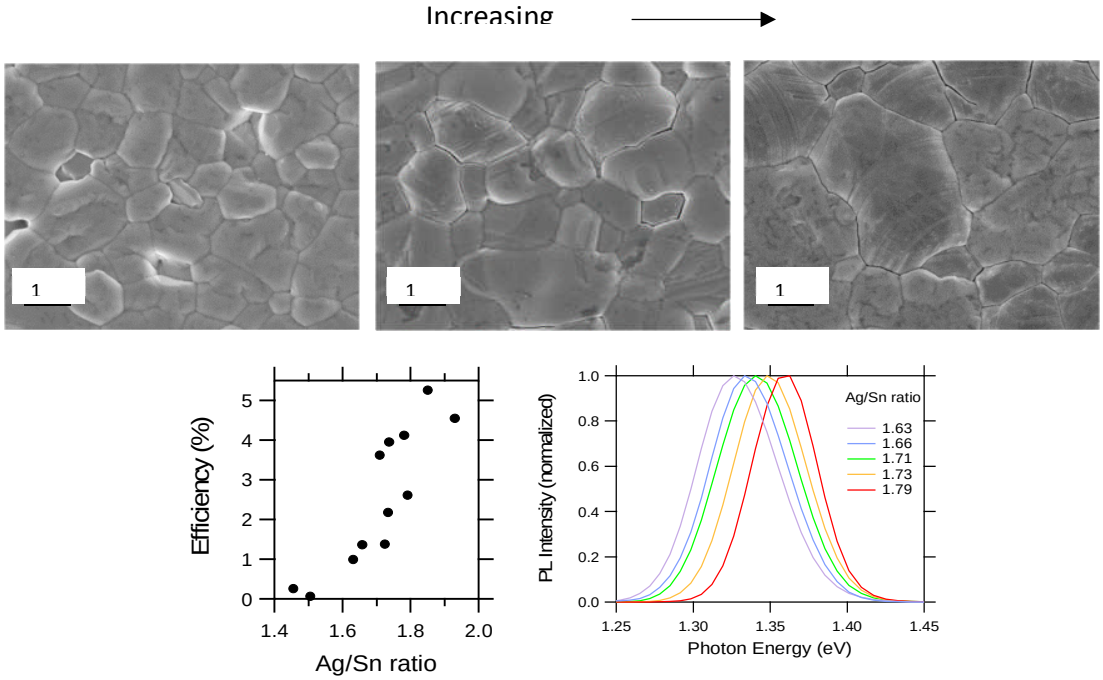

Figure 14: Top: The grain size of AZTSe is strongly influenced by excess Ag content in the absorber, which is believed to act as a flux agent during annealing. Bottom: Samples close to stoichiometry display the best performance and the highest photoluminescence emission energy, which is believed to indicate the cleanest band structure.

Finally, the loss mechanisms in AZTSe-based devices were studied. First, we found that the Schottky barrier height in AZTSe/MoO3 devices is only ~ 0.82V under illumination. This limits the maximum possible conversion efficiency (according to wxAmps simulations) to 6.4%. Better contact materials are therefore needed to achieve higher efficiency. Second, we found that the minority carrier lifetime in AZTSe-based devices is

very short (<225 ps). This was determined using two-photon spectroscopy, in collaboration with Ed Barnard at LBNL and Jeremy Poindexter from MIT. This short lifetime is incompatible with high-efficiency PV devices and must be improved. The extent to which this is limited by the bulk vs surfaces and grain boundaries is still unknown. Finally, we observe hysteresis in the J-V measurement. The application of reverse bias appears to shunt the devices. Careful pulsed electrical measurements reveal that this shunting is proportional to the duration and amplitude of the bias. We hypothesize that Ag^+ is mobile in AZTSe and that applying a negative potential to the MoO3 electrode causes Ag^+ doping of that layer[22]; thus, hysteresis is caused by reversible doping of the buffer which degrades the junction. When the bias is removed the resistance returns to the rest value. Thus, the mobility of Ag^+ ions could be problematic for the technology. All of these results are explained in detail in a manuscript, which has been submitted.

Tasks 4, 11, 17: Surface Modification and Alternative Buffers, Roy Gordon, Harvard

Thin-film solar cells may be described as containing an absorber layer covered by two buffer layers, one above it and the other below it. The absorber layer is a semiconductor that absorbs photons, thereby generating electrons in its conduction band and holes in its valence band. One buffer layer is designed to transmit the photo-generated electrons to an adjacent electrode, while blocking the photo-generated holes from entering that electrode. The other buffer layer is on the opposite side of the absorber layer. There it transmits photo-generated holes, while blocking the passage of electrons into the other electrode. Both buffer layers are semiconductor materials with wide band gaps, so that few, if any, photons are absorbed within the buffer layers.

This description using buffer layers gives a more helpful description of the operation of thin-film solar cells, for which the traditional p-n junction is a less appropriate model.

For these buffer layers to accomplish their required tasks, their band energies must be carefully chosen. An effective electron-transmitting buffer layer must have its conduction band energy close to that of the absorber layer, within a few tenths of an electron-volt. Thus the photo-electrons have an easy transit from the absorber layer through the buffer layer and into a collection electrode whose Fermi energy is not too far from either of these conduction band minimum energies. Because the band gap of the buffer is much larger (by at least 1 eV) than that of the absorber, the valence band energy of the absorber is much lower in energy, and thus the photo-generated holes cannot enter the buffer layer.

An effective hole-transmitting buffer layer has opposite properties. Its valence band maximum energy should closely match that of the absorber layer. Its conduction band energy should be far above that of the absorber layer, so that photo-generated electrons are blocked by this buffer layer.

Because the band energies of buffer layers must have the correct absolute band energies as described above, it is difficult to find a binary compound with the correct band energies. Thus the strategy in this research has been to use ternary compounds with wide band-gaps whose composition can be adjusted to give the optimum band alignments with the absorber layer.

Material	ZnO	ZnS	Ga_2O_3	In_2O_3	In_2S_3	SnO_2	GeO_2	CuI	CuBr	Cu_2O
Conduct. Band Min.	-4.5	-3.5	-3.0	-4.5	-3.5	-4.5	-3.0	-2.4	-2.9	-3.0
Valence Band Max	-7.5	-6.5	-7.8	-7.1	-6.1	-8.0	-8.0	-5.5	-6	-5.1
Band Gap	3.0	3.0	4.8	2.6	2.6	3.5	5.0	3.1	3.1	2.1
Type	n	n	n	n	n	n	n	p	p	p

Table 1. The buffer materials considered during this project. The values are in eV.

Atomic Layer Deposition (ALD) was chosen as the method for depositing these buffer layers because it provides good control over the stoichiometry of ternary compounds. ALD also makes layers with well-defined uniform thickness and composition even on surfaces that are relatively rough on an atomic scale. ALD processes were adapted from the literature in cases where an appropriate process had been reported: ZnO, ZnS, SnO_2, Cu_2O and CuBr. New vapor deposition processes were developed during the course of this project for Ga_2O_3, In_2O_3, In_2S_3, GeO_2 and CuI

The conduction band energy of CZTSSe lies at around -4 eV. Thus one can predict from the values in Table 1 that the following ternary compounds could be adjusted to have their conduction band minimum match that of CZTSSe: Zn(O,S), $In_2(O,S)_3$, and $(Sn,Ge)O_2$. On the other hand, $(Zn,Sn)O_x$ is predicted to have too low a conduction band energy, leading to a “cliff-type” band offset, which generally leads to lower solar cell efficiencies. In fact, experiments early in the program verified that CZTS cells with $(Zn,Sn)O_x$ n-type buffer layers had efficiencies below 4%. Modelling of these cells indicated that the conduction band minimum of $(Zn,Sn)O_x$ was in fact well below that of CZTS. Thus further work during this project concentrated on electron-transmitting buffer layers of Zn(O,S), $In_2(O,S)_3$ or $(Sn,Ge)O_2$. These materials could be non-toxic substitutes for the toxic cadmium sulfide currently used as a buffer layer in the most efficient CZTS solar cells.

Zn(O,S) with controlled composition was made by ALD from diethylzinc, water vapor and hydrogen sulfide. This buffer layer has been shown to be effective as an n-type buffer layer for solar cells with tin monosulfide, SnS, as the absorber layer. This ALD process has been described (reference: Prasert Sinsermsuksakul , Leizhi Sun , Sang Woon Lee , Helen Hejin Park , Sang Bok Kim, Chuanxi Yang , and Roy G. Gordon, *Adv. Energy Mater.* 1400496 (2014)), and it was shown that increasing the sulfur content increases the conduction band energy. During the early part of this program, CZTS solar cells were prepared with various S/O ratios, but none of them achieved efficiencies as high as the standard CZTS cells with CdS buffer layers.

The potential advantages of In_2S_3 as a buffer layer include its indirect band gap (meaning higher transmittance to the absorber than CdS) and the presence of comparatively less mobile In^{3+} ions (as against Cd^{2+}) under high temperature deposition conditions of CZTS-Se needed for the solar cells in the superstrate configuration. In previous work, chemical

bath deposited (CBD) In_2S_3 buffers showed a positive conduction band offset ("spike-type") of 0.15 eV. These films have an uncontrolled amount of oxygen and hydroxyl groups due to the solution-based deposition method. In_2O_3 is known to have a conduction band energy that is below that of CZTS. We conclude that pure In_2S_3 films have a conduction band minimum that is too high for optimum performance with CZTS. Tuning of the sulfur to oxygen ratio (S:O) can adjust the conduction band alignment with CZTS-Se at the p-n junction. This tuning is critical to obtaining cells with high efficiency. Thus we targeted making indium oxysulfide, $In_2(O,S)_3$, films with well-controlled compositions. Preliminary results for In_2S_3 films deposited at 150 ^oC were promising in terms of the band offset measurements (0.15 eV spike obtained by UPS; see Fig. X) and device performance.

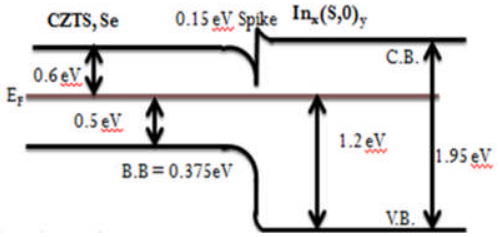

Figure 15 XPS determination of band positions for $In_2(S,O)_3$ on CZTS.

Under AM 1.5 illumination the films achieved a 5.83 % efficiency with a J_{sc} ,V_{oc}, and fill factor, of 37.3 mA/cm^2 , 433.5 mV and 36 % respectively. While the current outperforms CdS buffered devices, the voltage is 79.9 mV lower and the series resistance of the film is higher. The biggest deficits were in fill factor (33.8 % lower) and shunt resistance (200 ohm.cm^2 lower).. This indicated that band alignment of the film with CZTS-Se is not optimal and the film conductivity is too low. Handling these films in air (air exposure 2 days prior to measurement) likely introduced some oxygen contamination, leading to an $In_x(SO)_y$ composition. The above findings motivated us to investigate the controlled incorporation of oxygen in the film to obtain optimal electrical and optical properties of the buffer.

To provide a $In_2(O,S)_3$ buffer layers with a well-controlled composition, we developed an ALD process using a newly-synthesized, highly reactive precursor, indium tris(*N,N'*-diisopropylformamidinate), which makes pure thin films (free of carbon, nitrogen, oxygen, hydroxyl group and halide contamination). The O to S ratio was adjusted systematically by adjusting the ratio of ALD subcycles dosing the indium precursor and then water vapor or hydrogen sulfide. This ALD process produces $In_2(S,O)_3$ films with more homogenous composition than CBD, or post-deposition annealing in oxygen atmosphere. The ALD growth process produces very pure films at substrate temperatures from 150 to 200 ^oC with less than 1 atm. % carbon and nitrogen. Growth at a lower substrate temperature, 120 ^oC, produced carbon- and nitrogen-contaminated films, presumably due to incomplete removal of the ligands. We could controllably deposit compositions from pure In_2O_3 to oxy-sulfide alloys to pure In_2S_3.

The compositions measured by XPS and majority carrier properties measured by Hall characterization are shown in Table 2. The mixed compositions, highlighted in yellow, had similar mobilities. The films showed ~0.4 nm roughness by AFM and were found to be moisture resistant by XPS composition comparisons. TEM characterization revealed that while the In_2S_3 and In_2O_3 compositions were crystalline, the mixed compositions were

poorly crystallized. Despite this, mixed composition films exhibited relatively high mobility with a wide range of carrier concentrations.

Deposition Temperature (thickness, nanometers)	Composition By XPS (atom %)			Resisti-vity by 4 pt probe (ohm. cm)	Resisti-vity by Van der Pauw (ohm. cm)	Hall Electron Concen-tration (/cm^{-3})	Hall Mobility (cm^2/Vs)
	In	O	S				
200 C (Cubic)	**41**	**59**	**0**	**2.6e-3**	**2.4e-3**	**5e19**	**48**
200 C (Am.)	**41**	**49**	**10**	**1.7e-3**	**1.4e-3**	**4.3e20**	**10.9**
200 C (Am.)	**42**	**33**	**25**	**4e-2**	**2.9e-2**	**1.9e19**	**10.4**
200 C (Am.)	**44**	**17**	**39**	**-**	**22.7**	**4.7e16**	**9.1**
200 C (Am.)	**44**	**6**	**50**	**-**	**79.5**	**6e15**	**12.9**
180 C (Tetrag.)	**42**	**0**	**58**	**-**	**86**	**1e16**	**6**

Table 2. Composition and properties of $In_2(O,S)_3$ films.

UV-Vis Spectroscopy shows a higher band gap of ~2.4 eV for $In_2(O,S)_3$ films. Further work will be required to measure the band positions of these materials and to incorporate them into solar cells.

Tin germanium oxide, $(Sn,Ge)O_2$, films are another option for electron-transmitting, hole-blocking buffer layers. SnO_2 has a lower conduction band energy than CZTS, while GeO_2 has a higher conduction band energy. Thus the conduction band offset is raised by increasing the ratio of germanium to tin. By selecting an appropriate while the free electron concentration can be increased by fluorine doping.

An atmospheric pressure CVD process was used to deposit fluorine-doped $(Sn,Ge)O_2$ by the following reaction:

$(CH_3)_4Sn + (CH_3)_4Ge + O_2 + CF_3Br \Rightarrow (Sn,Ge)O_2{:}F$ + gaseous byproducts

Reactant gases were combined in varying ratios using a flow controller, and the resulting gas mixture was passed over a heated substrate. The tin and germanium precursor gases were prepared by injecting an evacuated gas cylinder with measured amounts of tetramethyltin or tetramethylgermanium and pressurizing the tank with nitrogen. Pure oxygen was used as the oxidant. Bromotrifluoromethane has been used to fluorine-dope tin oxide films in previous work, to increase the free electron concentration. Table 2 lists the typical deposition parameters, respectively.

A standard tin oxide deposition consists of a gas stream of 20 sccm oxygen, 13 sccm tetramethyltin (1.1 % in nitrogen), and a balance of nitrogen, delivered at 100 sccm. During tin-germanium oxide depositions, tetramethylgermanium (0.5 % in nitrogen) is added to the gas stream, and nitrogen is reduced by the sccm, maintaining 100 sccm total flow rate.

The germanium content in the film increases with the germanium precursor percent of total flow rate and with increasing substrate temperature. Table 3 below shows representative films that have been measured by RBS to determine their composition.

	"Low" Germanium	"High" Germanium
Deposition Temp.(C)	450	500
Ge:Sn Precursor Ratio	0.18	0.61
RBS Tin Content (at.%)	37	32
RBS Germanium Content (at.%)	0.55	7.5
Ge/(Ge + Sn) Ratio	0.015	0.19

Table 3. Composition of representative $(Sn,Ge)O_2$ films.

P-Type buffer layers were only studied toward the end of the project. They became more relevant when thinner CZTS absorbers were being studied. With a thinner p-type absorber layer, more photons reach the back contact. Thus having a buffer that can selectively transmit holes became helpful at the back contact. Also, later in the project, an n-type absorber, AZTS, was studied, in which silver substitutes for more than half of the copper. In this case, having a p-type buffer at the front contact becomes important. Thus p-type hole transmitting layers of CuI, CuBr, and Cu_2O were prepared. However, sufficient time was not available during this project to optimize the use of all these p-type buffer layers with AZTS.

p-type Buffer Layers for CZTS or AZTS

Copper(I) bromide, CuBr, and copper(I) iodide, CuI, were identified as potential p-type buffer layers with potentially high hole mobility. Their valence band edges should be adjustable in energy by the Br/I ratio: Br should lower the energy, while increasing the I content should raise it. However, no ALD process for CuBr or CuI has been discovered. Nevertheless, we were able to make these materials by a two-step process: ALD or Cu_2S followed by reaction with HBr or HI to exchange the sulfur with a halogen. This process is successful in making CuBr or CuI, but the resulting material readily agglomerates in

separate crystallites, rather than a continuous film. This kind of discontinuous layer is not suitable as a continuous buffer layer.

Cuprous oxide (Cu_2O), a p-type semiconductor material, is another potential p-type buffer layer for either CZTS or AZTS solar cells. Atomic Layer Deposition (ALD) and pulsed Chemical Vapor Deposition (CVD) processes for Cu_2O and Cu_2O:N have been developed. Bis(*N,N'*-di-*sec*-butylacetamidinato)dicopper (I), $[Cu(Bu\text{-}amd)]_2$, ammonia gas and water were used as the source of copper, nitrogen and oxygen respectively. $[Cu(Bu\text{-}amd)]_2$ is maintained at 120 ^oC in a glass bubbler and H_2O is maintained at room temperature. Electronic grade ammonia gas is used for N doping. High purity N_2 is used as the carrier gas and purge gas.

Nitrogen doping of Cu_2O is achieved by alternating ALD cycles of $[Cu(Bu\text{-}amd)]_2$ and H_2O with cycles of $[Cu(Bu\text{-}amd)]_2$ and NH_3. XPS quantification was carried out on and ALD film of Cu_2O:N (49:1). This film which has ALD cycle ratio of 49 to 1 is found to contain 2 at.% of N in it, which raises the p-type hole conductivity.

During the ALD process of Cu_2O, the deposition rate was measured to be approximately 0.05 A per ALD cycle. This ALD process allows very high control of its stoichiometry and film thickness during deposition due to its lower growth rate compared to the CVD counterpart.

To get the advantages of both ALD and CVD deposition processes, a pulsed CVD process was studied. Here, for a pulsed CVD cycle of Cu_2O, $[Cu(Bu\text{-}amd)]_2$ and H_2O are simultaneously provided in a pulse, followed by the purge with N_2 gas. For the pulsed CVD process of Cu_2O:N, additional cycles of $[Cu(Bu\text{-}amd)]_2$ and NH_3 in a single pulse are used. The pulse CVD process achieved a growth rate of 0.02 A per pulsed CVD cycle. This encourages the exploration of pure CVD growth processes for Cu_2O:N

The deposition of Cu_2O:N is found to be temperature dependent. At higher temperatures of 300^oC, the film is found to de-wet the surface and nucleate into hemispheres. By lowering the temperature down to 100-120^oC, we were able to achieve a smooth conformal film suitable for use as a buffer layer.

Large area, high throughput deposition of the buffer layers will enable Cu_2O to be feasible for large scale commercialization. Although we have achieved conformal growth of Cu_2O via the pulsed CVD method, a continuous CVD deposition process will allow this material to access a wider range of applications.

Compared to both the ALD and pulsed CVD processes, a continuous CVD process involves the continuous flow of both the metal-organic precursors and the oxygen sources which react/decompose on the heated substrates to produce the desired high quality and conformal solid thin film.

The copper metal precursor $[Cu(Bu\text{-}amd)]_2$ is maintained at 105 ^oC in a flow-through bubbler with a flow rate of 60 sccm. The oxygen source H_2O is maintained at room

temperature with 10 sccm of high purity nitrogen gas bubbled through the liquid using a dip tube. High purity ammonia gas is metered into the reaction chamber with a flow rate of 5 sccm. All the chemicals are precisely metered using calibrated units of Brooks 5820E thermal mass flow controllers and mixed sufficiently before injection into the reaction chamber. An exhaust throttling valve is used to maintain the chamber pressure at 3 Torr throughout the reaction.

The continuous CVD process for the synthesis of Cu_2O:N is capable of achieving significantly higher growth rates of up to 3 nm/minute. In comparison with previous synthesis processes, our continuous CVD method provides over 100 times more throughput. This allows the growth of a typical 10 nm thick Cu2O:N thin film to require only 3 minutes of deposition time.

Cross-section SEM images comparing Cu_2O:N film grown using the various vapor deposition methods shows film quality progressing as we move from ALD Cu_2O to pulsed CVD to continuous CVD Cu_2O. Film grains appear larger and the coating of the material becomes more conformal over the substrate.

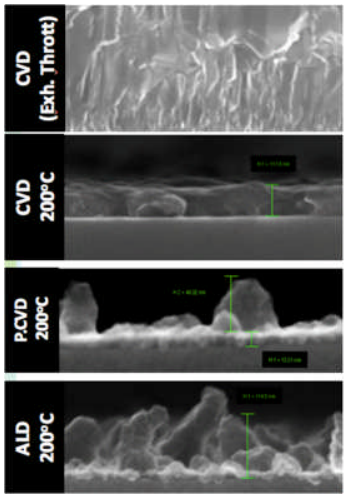

Fig. 16. SEMs of Cu_2O films. Bottom panel, ALD; next panel above, pulsed CVD; second from top panel, continuous CVD; top panel, continuous CVD at higher pressure.

In summary, deposition processes have been developed and tested for several potentially useful buffer layers consisting of wide-band gap semiconductos. N-type buffers include Zn(O,S), $In_2(O,S)_3$ and $(Sn,Ge)O_2$. P-type buffers include Cu(I,Br) and $Cu_2(O,N)$. None of these buffer layers have yet been demonstrated to increase the efficiency of CZTS or AZTS solar cells. However, with further optimization these new buffer layers may be able to increase the efficiency of these cells, or of other new absorber materials currently being developed, such as the perovskites.

Task 5: Surface Characterization, Richard Haight, IBM

Interfaces and Band Offsets

Another key issue involves the p-n junction, both in terms of the interface quality and the band offsets. In particular, for a high efficiency device, the conduction band minimum (cbm) of the n-type buffer (in this case CdS) must be slightly higher (spike) than that of the p-type CZTS,Se. At first blush one may question why a small barrier to electron flow from the absorber to the buffer is required. The reasons for this are two-fold. The first is that a buffer cbm below that of the absorber (cliff) can reduce Voc by enhancing e-h non-radiative recombination. Second, a spike offset removes electrons from the CZTS,Se/CdS interface and reduces the non-radiative e-h recombination that would dramatically reduce Jsc at the interface. Spike barriers up to ~0.4-0.5 eV are beneficial[23]; beyond this level higher barriers can reduce current flow and hence efficiency.

Measuring the band offsets between absorber and buffer typically involves sequential depositions of thin layers of buffer material followed by monitoring of the bulk atomic core levels with X-ray photoelectron spectroscopy (XPS) as they shift in response to charge transfer between buffer and absorber- band bending. This can be laborious and in the case of CBD deposition extremely difficult as the sample must be removed from the vacuum analysis chamber for each additional buffer deposition.

A unique approach (Fig.17) involves utilizing pump/probe femtosecond laser photoelectron spectroscopy or fs-UPS.[24] [25][26] The fs-UPS technique utilizes fs pulses from an amplified Ti:sapphire laser system whose output is split into ***pump*** and ***probe*** arms. The probe pulses are frequency upconverted to photon energies ranging from 15 to 40 eV for UPS by high harmonic generation in Ar gas; individual harmonics are spectrally selected and focused onto the sample in an ultrahigh vacuum analysis chamber and produce “standard” UPS spectra. To extract the band bending at the CZTS,Se junction, time-correlated 1.55 eV (800nm) pump pulses are focused on the probe area; the resulting dense e-h population created in the CZTS,Se screens the static dipole field in the depletion region and flattens the bands, causing a rigid energetic shift of the UPS spectrum. The laser intensity is sufficient to fully flatten the bands and the bending is extracted by measuring the magnitude of the shift.

Under flatband conditions the location of the clean CZTS,Se vbm can be determined relative to the Fermi level(Fig. 17) and the same for the CdS/CZTS,Se vbm. The cbm positions are then determined from the knowledge of the band gaps of both CZTS,Se and CdS as shown in the figure. This set of measurements provides the Fermi level of the system, band bending and valence band locations as well so that the electronic alignment of the system is fully determined. With this approach the band offsets have been determined for a series of buffer materials including CdS[25], ZnO, ZnS, In_2S_3 on CZTS,Se[26] and Zn(O,S)/SnS[28].

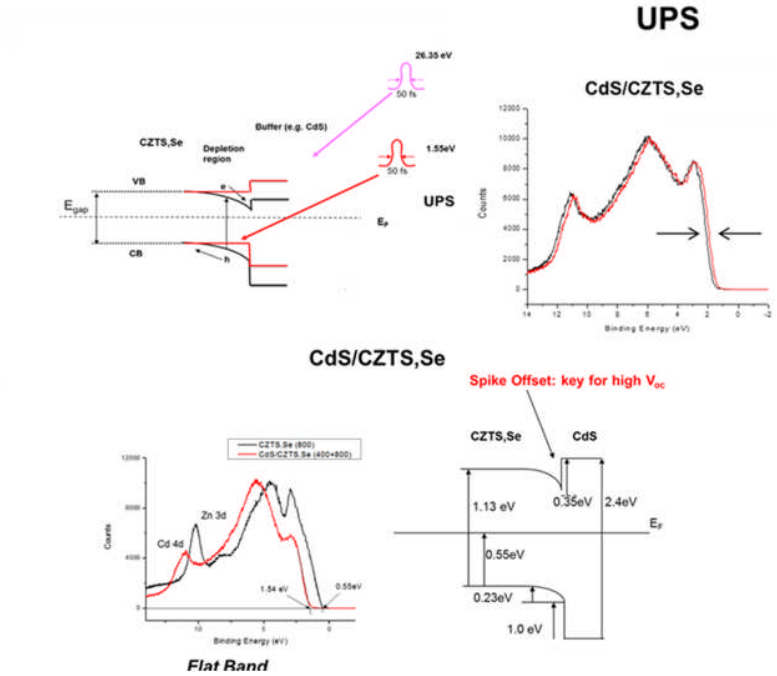

Fig. 17. Top: band schematic showing the junction region. 1.55 eV pump photons flatten the bands while a time synchronized 26.35eV pulse of light is used for UPS. Below shows the comparison of unpumped(black) and pumped (red) spectra. Bottom left: overlap of flatband bare CZTS,Se (black) and 20 nm CdS/CZTS,Se. Right: band diagram with band bending extracted from the spectral data.(Ref.[27])

Task 12: High WF Back Contact and Superstrate Results, Richard Haight, IBM

Back Contact Engineering

Now that bulk defects, interfaces and grain boundaries have been studied and discussed in considerable detail, and their impact on device performance is arguably better understood, we focus on ways to improve the efficiency of CZTS,Se based solar cells. One approach is to address the key issue of bulk defects that, as we have discussed result in band tails that narrow the band gap and lower Voc. One approach to mitigating the formation of Cu-Zn antisite defects is through the incorporation of Ag whose larger covalent radius increases the barrier to antisite formation. This will be discussed in the next section. Another approach is through back contact engineering involving the imposition of an electrostatic field that drives the separation of electrons and holes and this is discussed in this section.

The physics of back contact engineering is captured in Fig. 18 below. In essence, a high work function material such as MoO_3 deposited onto the back of CZTS,Se results in electron transfer from CZTS,Se to the MoO_3 as the Fermi levels of the two materials equilibrate. This in turn generates an electrostatic field within the CZTS,Se that drives electron away from this interface and toward the p-n junction. Fs-UPS confirms that this charge transfer and subsequent band bending does indeed occur.

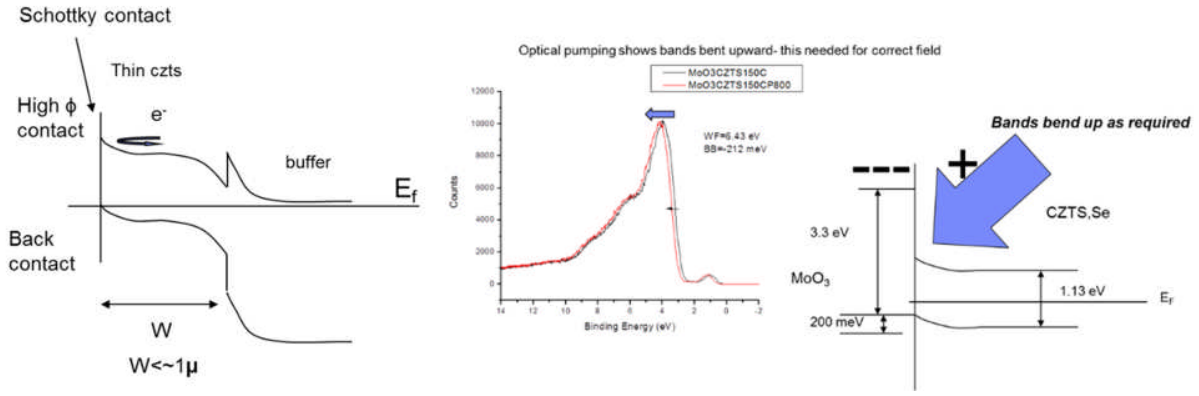

Fig. 18. Top: Schematic showing band bending near rear surface of device associated with electron transfer from the lower work function CZTS,Se (5.2eV) to the high work function MoO_3(6.5eV). Bottom left: fs-UPS showing that the bands bend upward at the MoO_3 interface. Black spectrum is unpumped and red spectrum is pumped CZTS,Se. The shift to higher binding energy following pumping indicates the bands are originally bent upward. The direction and magnitude of the band bending are shown in the bottom-right schematic.

As can be seen from the spectrum (Fig. 18) pumping of the MoO_3/CZTS,Se interface shifts the spectrum to higher binding energy indicating that the unpumped bands are bent upward. The upward band bending is a result of an electrostatic field that drives electrons toward the front of the device creating an electron mirror that increases Voc and reduces recombination at the back interface.

With the presence of a field at the back contact, the question as to how to further capitalize on this effect arises. In order for an increase in Voc and hence efficiency to occur the absorber thickness must be tailored to exploit this. Two additional factors must be accounted for, including the carrier diffusion length and the depletion width near the p-n junction. As a result the absorber thickness (L_{abs}) must be smaller than the sum of the front contact depletion width (L_{depF}), back accumulation width (L_{accumB}) and the carrier diffusion length (L_{diff}). We can write a simple equation that states

$$L_{abs} \leq L_{diff} + L_{depF} + L_{accumB}$$

L_{diff} ~ 1μm [29] while the depletion width near the p-n junction is 200-300 nm and accumulation width <100 nm near the back contact. This implies that the absorber thickness must be below ~1-1.5μ before increases in Voc would be noticeable. This result is confirmed with device simulations (WXAmps)[30][31], shown in Fig 19. At 2 μm absorber thickness little difference is observed between the high work function (HWF), reflective back contact and the standard Mo back contact. But below ~1.5μm WXAMPS predicts a continuous increase in Voc, with substantial increases occurring below 1 μ.

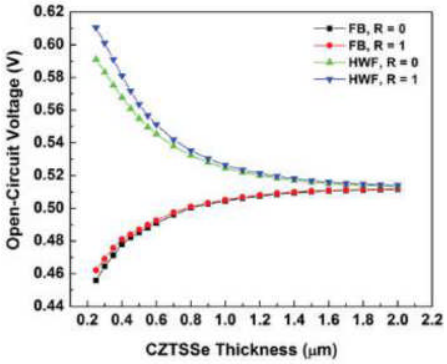

Fig. 19. WXAmps device simulations comparing Voc for a standard PV device (black squares and red circles) as the absorber is thinned and one with a high work function back contact (green and blue triangles). FB refers to flat band (MoS_2 or $MoSe_2$) and reflectivities (R) are either 1 for a highly reflective back contact or 0 for a non-reflecting contact.(after Ref.[30])

Although back contact modification can be carried out in the "substrate" mode where the CZTS,Se is deposited atop the HWF layer, the required high temperature anneals to crystalize the CZTS,Se results in degradation of the layer due to elemental diffusion. To deal with this issue, we instead grow a full CZTS,Se solar cell and separate (exfoliate) the active device from the Mo/glass substrate. In this "superstrate" process, a thin piece of fused silica is epoxied atop the device and exfoliation is carried out with a mechanical impulse.

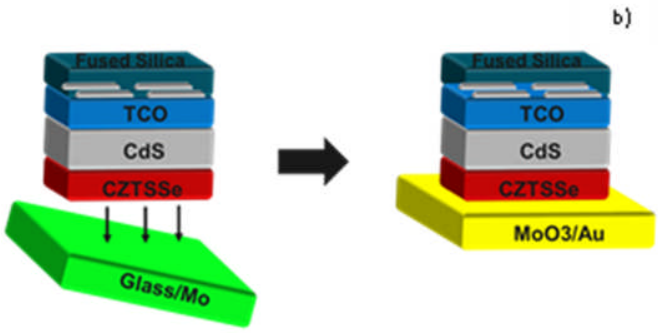

Fig. 20. Schematic showing process by which the CZTS,Se PV device is removed (exfoliated) from its Mo/glass substrate, followed by deposition of a high work function MoO_3 layer plus Au.

This process exposes the back surface of the CZTS,Se absorber and experiments have shown that no residual Mo is present. A new back contact consisting of a 10-70 nm MoO_3 layer and a thicker layer of Au are deposited at or near room temperature as shown in the Fig. 20 and additional "superstrate" measurements are carried out.

Actual measurements of Voc, as shown in Fig. 21 reveal that Voc increases with decreasing absorber thickness. The data (black squares) all lie below the actual WXAmps simulation suggesting that this difference arises from the lack of complete passivation of the back surface in the actual devices.

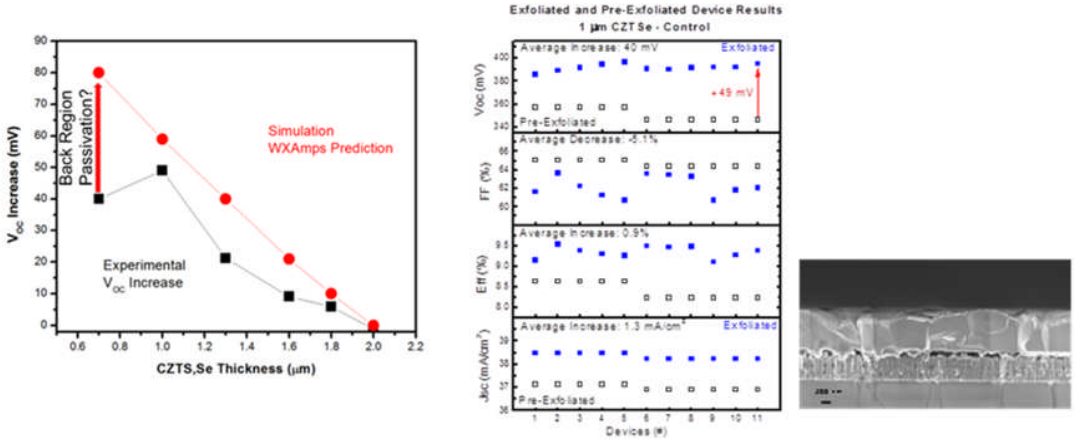

Figure 21. Left: Comparison of WXAmps simulation (red) and experimental exfoliated device results for Voc for increasingly thinner CZTS,Se films with high work function, reflective back contacts. Middle: Results comparing exfoliated devices with a high work function and reflective back contact (solid blue boxes) and pre-exfoliated devices with a standard flat band contact (open black boxes), Right: Cross-sectional SEM image of a representative 1 µm CZTSSEe absorber.

Recent results have shown all-around improvement in device performance including Voc, fill factor (FF), Jsc and efficiency. In addition to the increase in Voc as we have just described, FF improves due to the removal of the original back contact that may contain secondary phases that lead to increased non-radiative e-h recombination and hence reduced series resistance. Jsc is observed to improve due to the index matching properties of the epoxy that reduce reflection of incoming light. Exfoliation and Back Contact Engineering- Utilizing high work function back contacts to increase Voc

We have made significant advances in improving our exfoliation and back contact engineering. Fig. 22 shows a J-V curve with 11% efficiency and Voc=552mV. Incorporation of S into the hard bake process has been used to fabricate higher Voc devices exhibiting > 11% efficiencies from 500mV to 670 mV. These advances include:

- Increases in Voc by incorporating S into the hard bake process in a controlled fashion to achieve 650-670 mV Voc at 11.4% efficiency in exfoliated device
- Use of B-doped CdS to increase blue light penetration into absorber
- Use of AR-coated fused silica as cap when epoxying to device before exfoliation
- Continued use of MoO_3 +Au back contact
- Use of $(NH_4)_2S$ as back contact treatment before deposition of MoO_3 and Au

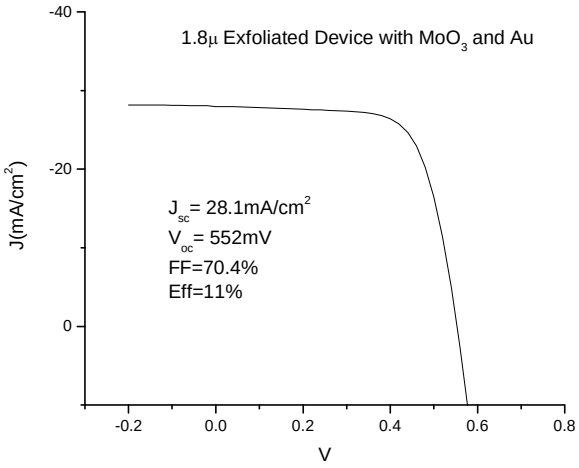

Fig. 22. J-V curve for 11% exfoliated device with 553 mV Voc and FF>70%.

Pre-exfoliated <Voc>=549.6 mV, Exfoliated <Voc>=553.2mV- increase of 3.6mV. For 2 μ thick devices this increase in Voc is what is typically expected. Figure 5 shows the J-V results for an 11% exfoliated device with MoO_3 +Au with high Voc and a FF>70%. Fig. 23 below shows pre-DoE device performance (color coded, >1000 devices) and recent device YL-63-A1. A number of devices showed equivalent performance. The YL-63-A1 device Voc deficit sits well below the previous device performance and is close to the predicted value for a uniform sample with band tailing parameter of 85 meV. YL-63 device is represents a significant improvement in Voc deficit.

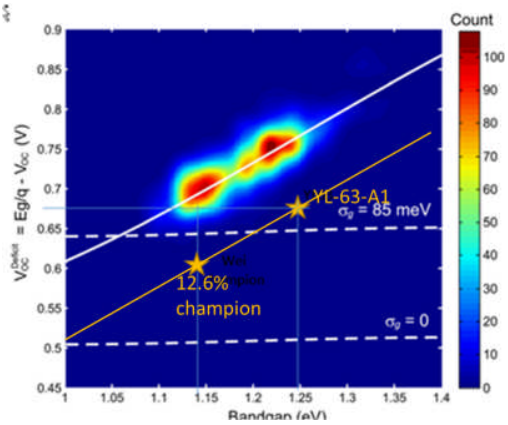

Fig. 23. Chart from Gokmen, et. al. APL103, 103506 (2013) with both 12.6% champion and recent YL-63 device superimposed showing >100mV improvement in Voc deficit.

Fig. 24 below shows achieved efficiencies, FF, Voc and Jsc for 1.1 micron devices with various back surface treatments.

PCE %	FF %	V_{OC} mV	J_{SC} mA/cm$_2$	Treatment	Thick um
12.2	69	467	38	Se (10 nm)	1.1
11.6	68	449	38	Al_2O_3 1 cycle, taped	1.1
11.2	66	443	38	Ozone	1.1
11.1	67	439	38	KCN	1.1

Fig. 24. Highest efficiencies achieved with various treatments of back surface prior to MoO_3 +Au back contact deposition.

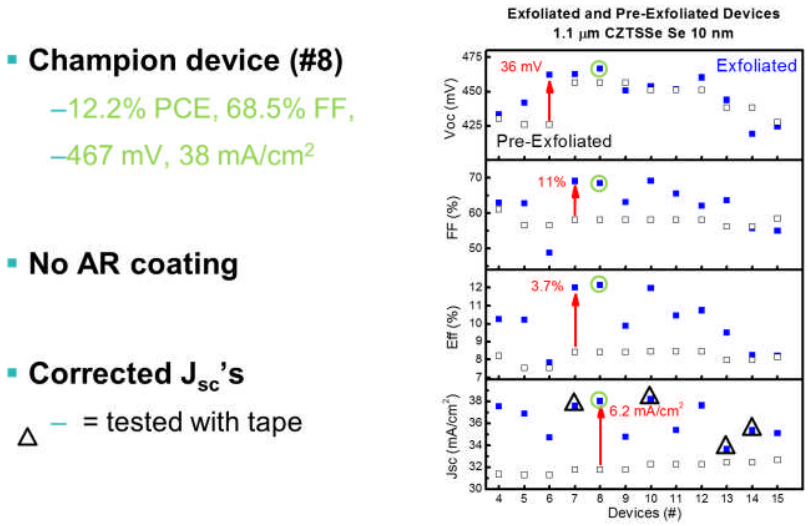

Fig. 25. Highest exfoliated efficiency of devices with Se at back contact is 12.2%.

Figure 25 shows the improvement in device performance following exfoliation with a 10 nm layer of Se which provides a level of back surface passivation. Masking to prevent light penetration outside of the active device area was carried out and resulted in a 12.2% efficient device with a FF=68.5%. Additional experiments on back surface passivation have been carried out to further reduce e-h recombination with the intent to increase Jsc and Voc. To this end PL experiments on the back surfaces of exfoliated films were carried out following different etches including ammonium hydroxide, sulfide and KCN. Both KCN and ammonium sulfide are known to remove secondary phases in the form of metal selenides. Ac can be seen in Fig. 26 ammonium sulfide and KCN led to the highest PL while ammonium hydroxide which typically only removes oxides and the control samples exhibited the lowest PL. Higher device performance is correlated with ammonium sulfide and KCN treatments.

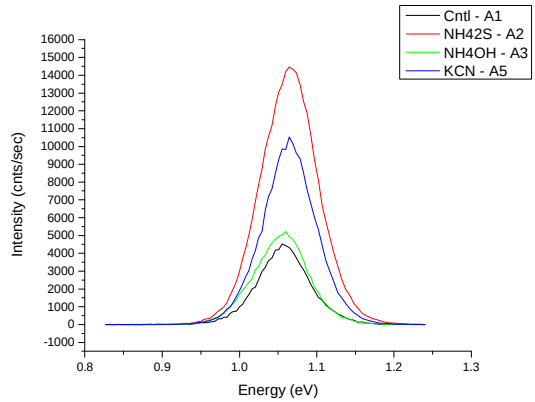

Fig. 26. PL intensities for various back surface passivation experiments including ammonium hydroxide, sulfide and KCN. Ammonium sulfide and KCN showed the highest intensities correlating with effective removal of secondary phases.

Additional experiments included carrying out air anneals in low humidity environments which improved overall efficiency, slow cooling following air anneal which improved Voc with a slight degradation of FF.

Task 6, 12, 18: Bulk Characterization, Oki Gunawan IBM

The task goals consisted of the following:

- Perform battery of tests on record devices : temperature-dependent J-V, quantum efficiency, capacitance, Hall effect, temperature dependent PL and TRPL, + structural characterization such as SEM, TEM, and XRD.
- Establish the impact of defects (incl. secondary phases)
- Combine all the optimization studies to push efficency to >18% with Voc deficit<475 mV

Task Results Summary:

(1) Characterization of New Champion (2015) Voc Deficit CZTSe

In 2015, we produced a new record Voc deficit CZTSe (no sulfur) by thermal co-evaporation process with Voc deficit of 577 mV, Eg = 1.0 eV and Eff = 11.6% (certified). We perform detailed characterizations as reported in[32] and highlighted in Figure 27. Notable features are large grain size (2 - 4 μm), record minority carrier diffusion length of Ld = 2 μm and high electron mobility of 560 cm^2/Vs.

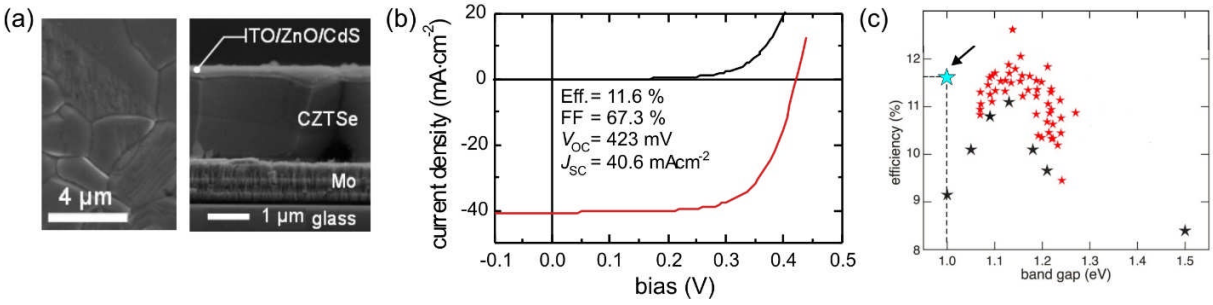

Figure 27. (a) SEM images (b) I-V (c) Efficiency vs. bandgap indicating the new record device.

(2) Comprehensive bandgap-dependent & Fill factor study of CZTSSe with varying S/(S+Se)

We investigated the effect of S/(S+Se) ratio or bandgap as they strongly influence the CZTSe device characteristics. We have performed various characterizations based on a set of CZTSSe that spans all possible bandgaps (1.0 – 1.5 eV). Characterizations include physical (XRD, Raman), optical (absorption, reflectivity, PL/TR-PL) and electrical (I-V-T, capacitance, suns-Voc and QE). The CZTSSe bandgap dependence is summarized in Fig. 28. There are various competing effects as the S/Se or bandgap increases: (1) Increasing Voc. (2) Lowering of carrier density that increases series resistance and lower FF. (3) Reduction in dielectric constant that makes screening less efficient thus increasing tail states & increases Voc deficit (4) Reduction in collection length that reduces the quantum efficiency and Jsc. These various competing effects lead to a curious property: the peak efficiency of CZTSSe that occurs at the close bandgap as CIGS at ~1.15 eV.

We have also investigated the comprehensive FF dependence on the bandgap (Fig. 29). Monochromatic high intensity Suns-Voc study reveals non-ohmic back contact problem at high bandgap CZTS where the Suns-Voc curves bend. Hall study reveals lower carrier density at higher bandgap leading to higher series resistance while mobility is approximately constant. We have also performed detailed study on the impact of secondary phases in CZTSSe with varying S/(S+Se) ratio; one of the main finding is that by increasing S/(S+Se) besides increases in the Voc deficit, the device also tend to have lower carrier density and more harmful secondary phases that increases series resistance and produces non-ohmic back contact. This serves as competing factor that lowers the FF at high bandgap leading to optimum device performance around 1.1 eV. This work is summarized in book chapter and Ref. [33]

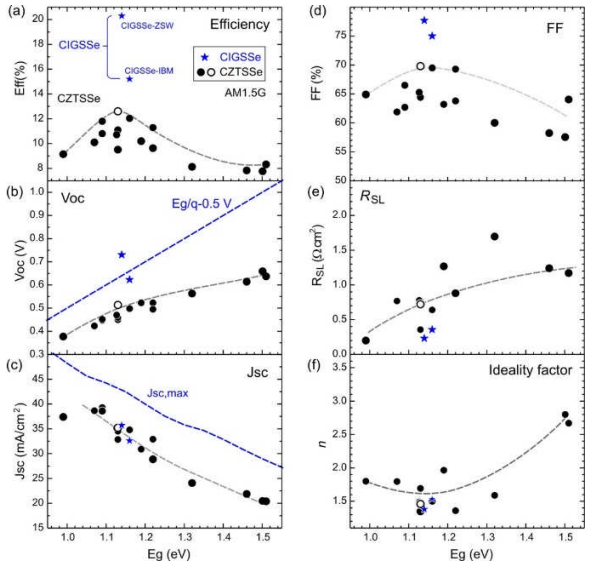

Figure 28. Summary of bandgap dependence in CZTSSe [2]: (a) Efficiency (b) Voc (c) Jsc (d) FF (e) Series resistance under light and (f) Ideality factor

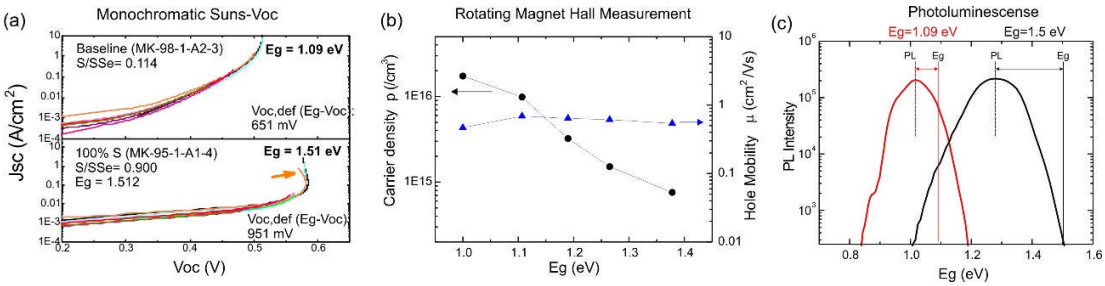

Figure 29. CZTSSe FF study: (a) Monochromatic Suns-Voc showing non-ohmic back contact problem at high bandgap. (b) Hall measurement vs bandgap. (c) Photoluminescense spectra at two bandgaps.

(3) CZTSSe Exfoliation Technique for Back Contact Engineering

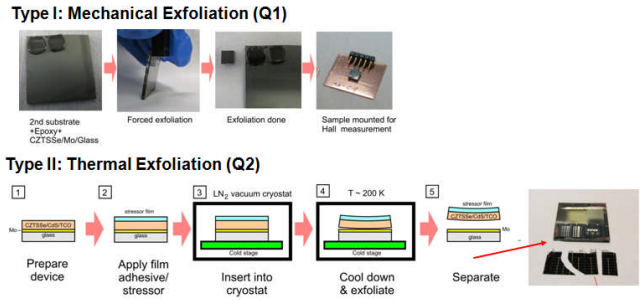

Figure 30. Exfoliation technique: (a) Mechanical (b) Thermal

We have developed two kinds of exfoliation techniques: (I) Mechanical exfoliation; where a small secondary substrates are glued with epoxy to the absorber and then they are knocked away thus removing the absorber from the underlying Mo metal. (II) Thermal exfoliation; using acrylic film pasted on the absorber and cooled down the system to 200K for exfoliation Fig. 30. These two techniques are very useful for back contact engineering study in this project.

(4) CZTSSe Electronics Defect Study by Photoluminescence

We performed extensive electronics defect study by photoluminescense (PL) of CZTSSe vs. CIGSSe to gain deeper understanding of the electronics defects that impact the Voc deficit. We used high performance CIGSSe devices (Eff ~ 15%) and a low (1.09 eV) and high (1.49 eV) bandgap CZTSSe. We performed PL (that yields spectra) and time-resolved PL (that yields lifetime) vs. laser intensity and temperature as summarized in Fig. 31. From excitation-dependent PL, the total defect density (which include radiative and non-radiative defects) within the band gap (Eg) was estimated for each material and the consequent depth of the electrostatic potential fluctuation (γ) was calculated. The quasi-donor-acceptor pair (QDAP) density was estimated from the blue-shift magnitude of the QDAP PL peak position in power-dependent PL spectra.

Band tails induced by unscreened charged defects are described by the depth of the fluctuating potential (γ). The total defect density (N_t) and QDAP density were estimated and found to be: CIGSSe < CZTSSe1 < CZTSSe2 where CZTSSe2 has higher S/(S+Se) ratio than CZTSSe1. A direct measurement of the lifetime at different photon energies ($d\tau/dE$) reflects the degree of carrier localization and therefore it qualitatively gauges the magnitude of γ. With increasing defect density, larger γ results in a deeper penetrating tail states inside the band gap, which effectively reduce the achievable V_{OC}, i.e. increases the V_{OC},def. Lastly, the stronger PL intensity loss with increasing temperature and higher activation energies (*Ea*) in both CZTSSe samples. This study suggests that, compared to CIGSSe, CZTSSe has more non-radiative recombination centers and also deeper defect states. Thus further improvement in CZTSSe should focus on reducing these defects and tail states. This work is published in Ref. [16]

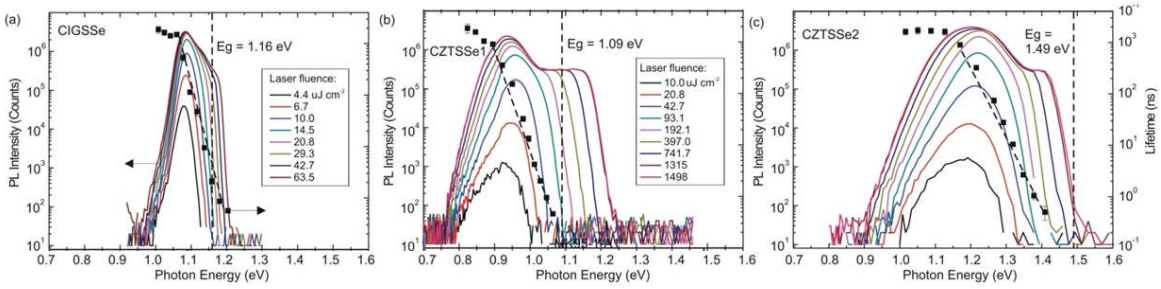

Figure 31. *Power-dependent photoluminescence (left axis) recorded at 7K for (a) CIGSSe (Eg =1.16 eV) (b) CZTSSe1 (1.09 eV) and (c) CZTSSe2 (1.49 eV). The vertical dashed line corresponds to the band gap (E_g). The black square symbols are the recombination lifetimes from time-resolved PL at different photon energies (right axis)* [5].

(5) Characterization of champion ACZTSSe device

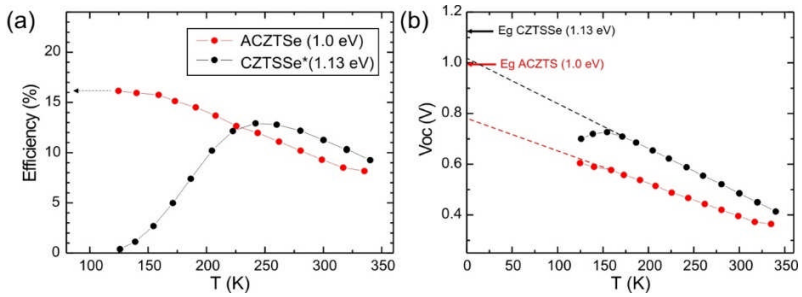

Figure 32. (a) Efficiency vs temperature for current champion ACZTSSe (~10% at 300K) and the world record CZTSSe (12.6% at 300 K).

We studied the low temperature characteristics of our recent champion AgCuZnSnSSe (ACZTSSe). We observe the promising result that the efficiency of the ACZTSSe sample does not collapse at low temperature. It reaches 16.2% at ~125 K (Fig. 32) which is the highest low temperature ever recorded so far for any kesterite and alloys. For example, the world champion CZTSSe (Eff ~ 12.6%, Eg=1.13 eV) shows efficiency collapse at low temperature. This is an encouraging result as the low temperature device performance sets the upper bound of the device performance at higher temperature - and point to the fact that by alloying ~10% Ag we can alter the bulk property of the device in positive way. Further capacitance study yield high charge density of $4x10^{16}$ /cm^3 in the absorber, consistent with the Hall measurement data of p = $3x10^{16}$ /cm^3. This suggests that the Ag alloying increases the carrier density and has shallow acceptor level, consistent with the fact that the carriers are not frozen out at T ~125 K - thus giving higher efficiency. Note that this high carrier density behavior are also observed in high Cu samples i.e. Cu/(Zn+Sn) ~ 1 but they never yield efficiency higher than 10% at any temperature. The result is reported in Ref.[18].

(6) Development of High Sensitivity Rotating Parallel Dipole Line Hall System

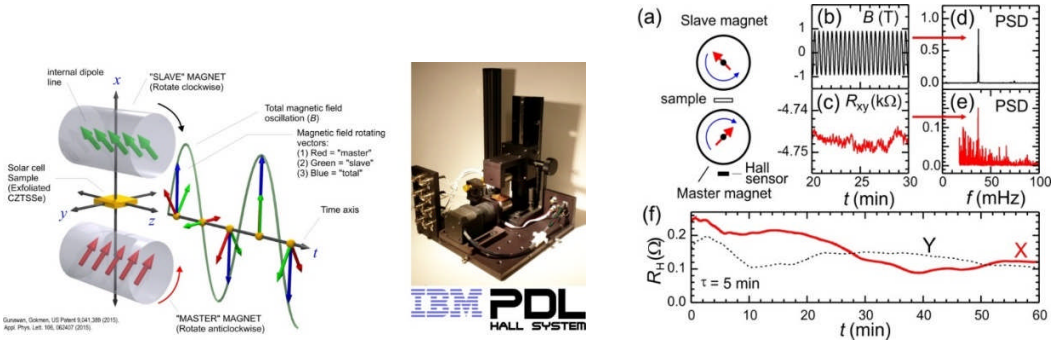

Figure 33. High sensitivity rotating PDL Hall system[34]: (a) Schematics (b) Machine setup. (c) Measurement examples.

Hall measurement is very important in characterizing the solar absorber to obtain the type, density and mobility of majority carrier, unfortunately low mobility values in most PV thin films result in very small and noisy Hall signal. Throughout the project we have developed and improved our unique rotating “Parallel Dipole Line” (PDL) Hall system (Fig. 33). The system is based on rotating PDL magnetic trap design combined with Fourier analysis and lcok-in detection technique. The system has played decisive role in extracting the CZTS mobility and carrier density: p ~ 0.5 cm^2 V/s (10x smaller than CIGS), served important role for alloying study: Ag, Mn, S/(S+Se) study and attracted a lot of external and commercial interest in the PV community. The result is reported in Ref.[34]. Recently

we have also discovered a new capability with this system: we can perform a *carrier-resolved* photo-Hall measurement and parameter extraction (mobility & density for both majority and minority carrier separately). The new key ingredients are the pure harmonic ac field generation with the PDL system and 2nd harmonic detection of the longitudinal magnetoresistance. Publication is in progress.

Task 13: CryoFIB and NanoAuger, Andrew Kummel, Kasra Sardashti UC San Diego

Cross-sectional NanoAuger studies have been performed on CZTSSe thin films, in order to determine the structure and composition of the back contact layer. Smooth cross-sections have been milled using cryogenic focused ion beam (Cryo-FIB) at 90 K with 5º ion beam angle of incidence. NanoAuger elemental maps for the CZTSSe/Mo interface (Figure 34a) showed the presence of a thick Mo(S,Se)y layer in between CZTSSe and Mo. In addition, there were some voids at the back interface where the signal for all seven elements was attenuated. The NanoAuger line trace at the back interface (Figure 34b) for confirms presence of an interfacial layer between Mo and CZTSSe, rich in Mo, S and Se. Cross-sectional kelvin probe force microscopy (x-KPFM) measurements on the same interface showed that this interfacial layer has higher work function therefore inducing an upward band bending in the CZTSSe. These results were consistent with good performance of the CZTSSe device grown directly on Mo. However, presence of voids could hinder further boost in the efficiency and Voc particularly for thinner films. Therefore, performing exfoliation and back surface clean (CMP or chemical etch) is necessary for CZTSSe films below 2 µm thickness.

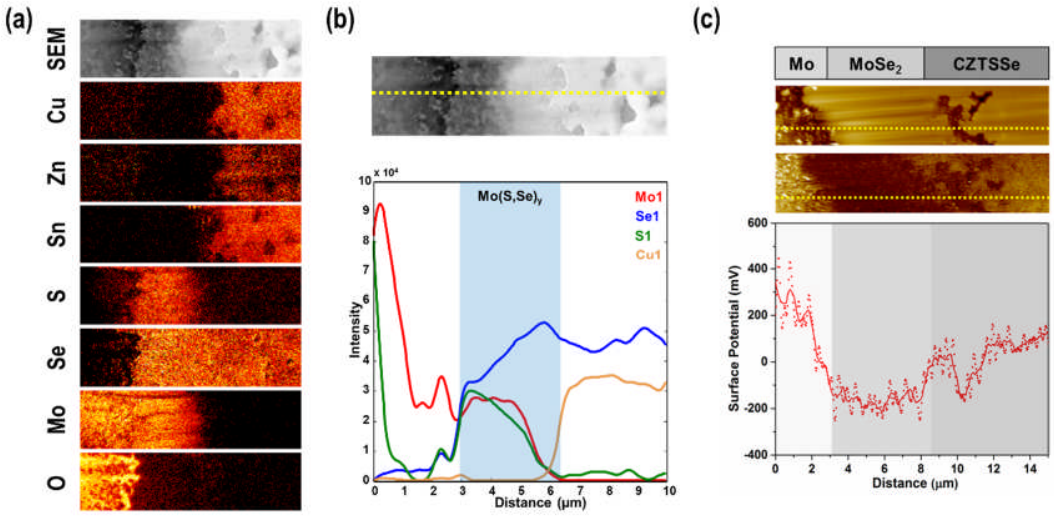

Figure 34: Cross-sectional NanoAuger on CZTSSe / Mo interfaces prepared by grazing angle Cryo-FIB: (a) SEM micrograph and elemental maps; (b) Line trace for Mo, Se, Se and Cu. X-KPFM surface potential map and line trace for the same cross-section is shown in (c).

A comprehensive set of cross-sectional KPFM (x-KPFM) studies has been performed on CZTSSe and AZTSe thin films. Smooth cross-sections were fabricated using cryogenic focused ion beam (milling at of 80 – 100 K) with 5º ion beam angle of incidence. KPFM measurements were performed on the cross-sections under Ar atmosphere. Cross-sectional surface potential maps (Figure 35a and 35b) showed a region of smaller potential (larger work function) between Mo and both AZTSe and CZTSSe. This is consistent with the formation of a thin MoSe2 layer which induces upward band bending within the absorber adjacent to the back contact. However, unlike CZTSSe, because of the of the n-type nature of AZTSe upward band bending is not favorable on the back side of the films. Alternatively, FTO substrates have been used for AZTSe. X-KPFM measurements on AZTSe / FTO interface (Figure 35c) showed downward band bending that is beneficial for electron extraction on the back side of the devices. These results were consistent with remarkably higher performance of AZTSe/FTO device in comparison with AZTSe/Mo.

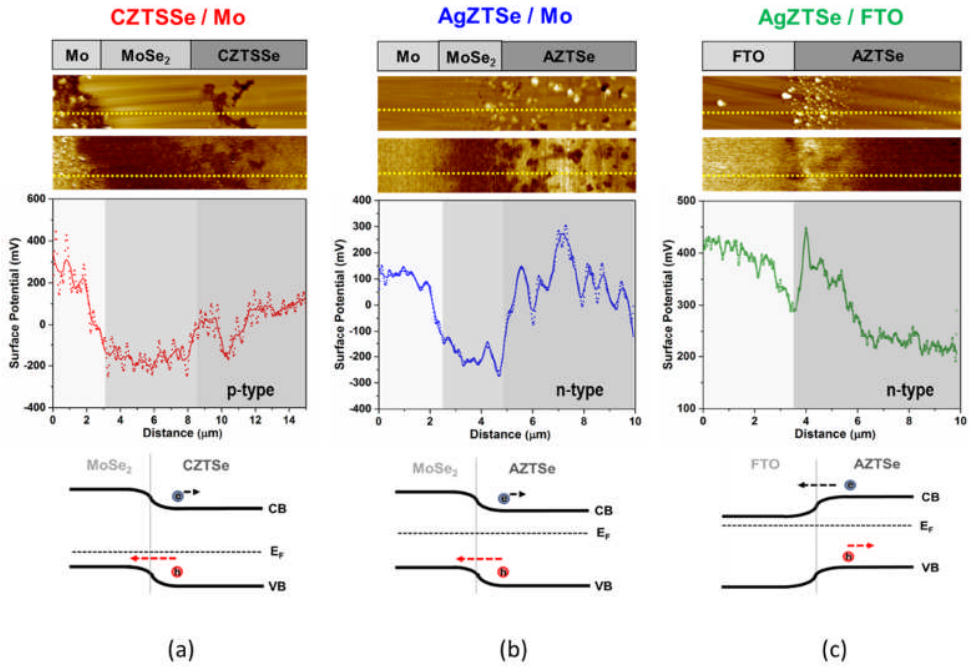

Figure 35: Cross-sectional Kelvin Probe Force Microscopy (x-KPFM) on the back side of (a) CZTSSe / Mo, (b) AZTSe / Mo and (c) AZTSe / FTO thin films.

Cross-sectional NanoAuger studies have been performed on exfoliated CZTSSe thin films, with MoO3 hole contact layer, in order to determine the structure and composition of the CZTSSe / MoO3 interface. Smooth cross-sections have been milled using cryogenic focused ion beam (Cryo-FIB) at 90 K with 5º ion beam angle of incidence. NanoAuger elemental maps for the CZTSSe/Mo interface (Figure 36a) showed the presence of a thin MoOx layer in between CZTSSe and Au. Large interface roughness is obvious in the elemental maps consistent with large void density near the CZTSSe back surface prior to exfoliation. Cross-sectional kelvin probe force microscopy (x-KPFM) measurements on the CZTSSe / MoOx / Au interface showed very large work function

difference between the contact layer and absorber, inducing a significant upward band bending in the CZTSSe (Figure 36).

While this large band bending could improve the performance, presence of voids and surface recombination centers near this interface could hinder further V_{oc} boost particularly for thinner films. Therefore, performing exfoliation and back surface clean (CMP or chemical etch) is necessary for CZTSSe films below 2 µm thickness.

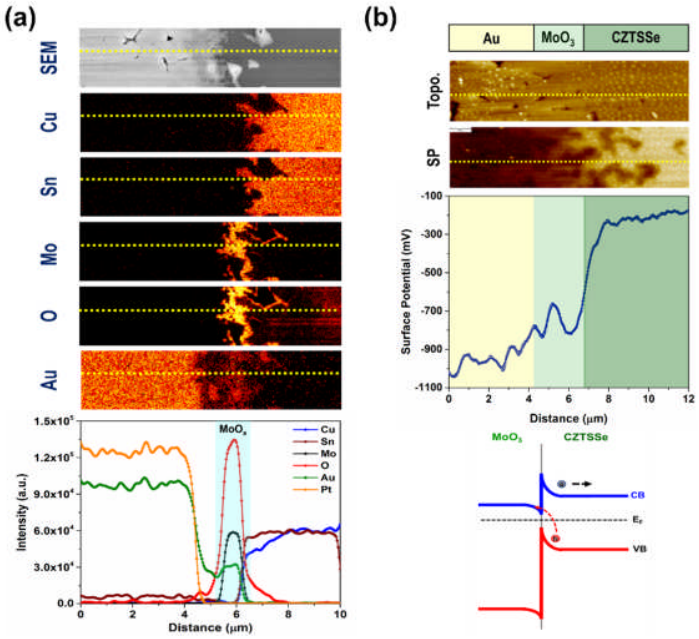

Figure 36: Cross-sectional NanoAuger on CZTSSe / MoOx / Au interfaces prepared by grazing angle Cryo-FIB: (a) SEM micrograph and elemental maps as well as a line trace for Cu, Sn, Mo, O, Au and Pt. X-KPFM surface potential map and line trace for the same cross-section is shown in (b).

Tasks 7, 8, 14, 19: Modeling of Isolated Defects/Grain Boundaries, Andrew Kummel, UC San Diego

High temperature phase stability of the CZTS-Se alloy

In CZTS-Se, a substantial portion of the Voc deficit is thought to be due to the Cu-Zn exchange sites; Cu and Zn are known to have nearly random locations in CZTS-Se grown at high T. Calculations were performed to deduce if these Cu-Zn sites could be removed by slow cooling and calculations were performed to determine if isoelectronic or isovalent substitutions could raise the energy of the metal exchange defect sites thereby reducing their density. Three sets of calculations were performed: (a) Determination of the role of Cu-Zn exchange in CZTS-Se stability to evaluate the possible effects of slow cooling on $CZTS_{0.25}Se_{0.75}$ Voc; (b) Calculation of the electronic structure and defect energies in $AgZTS_{0.25}Se_{0.75}$, and (c) Calculation of the electronic structure and defect energies in $CuMnTS_{0.25}Se_{0.75}$.

CZTS-Se Stability at High T: As shown in Fig 37, the phase stability of $CZTS_{0.25}Se_{0.75}$ was calculated with vibration / heat contribution to Gibbs energy (Gvib) and Cu-Zn and

S-Se intermixing contribution to Gibbs energy (Gmix+Gvib) versus the only Gmix mixing contribution. (Note: all Gibbs energy values include formation energy term.) There is finite stability even with only Gmix although it has a reduced range of chemical potentials. As shown in Fig 38, the phase stabilities (change of Gibbs energy) of $CZTS_{0.25}Se_{0.75}$ and CZTSe to decomposition to the primary decomposition products were calculated as a function of temperature including the effects of Gmix only, Gvib only, and Gmix + Gvib. For $CZTS_{0.25}Se_{0.75}$, if Gmix is removed by slow cooling, CZTS-Se shows very minor propensity to decompose of only 0.02 eV For CZTSe (no sulfur), without Gmix, there is a weak stability. This is consistent with Nano-Auger experiments readily showing secondary phases for CZTSe but no secondary phases for CZTS-Se.

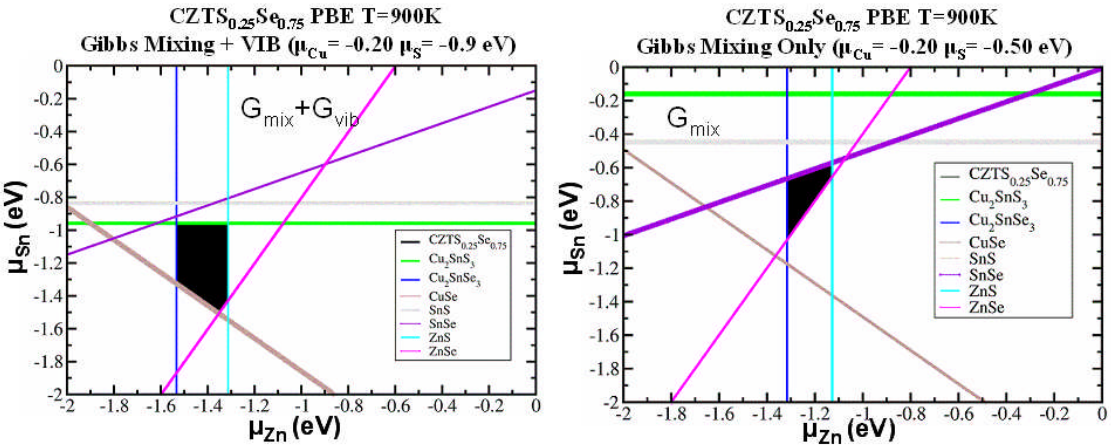

Figure 37. Phase Diagrams for $CZTS_{0.25}Se_{0.75}$ with/without Gvib at constant Cu and S potentials at 900K. Gmix at T=900K is included in both cases. Removal of Gvib lowers phase stability but there is still a large range of chemical potential over which $CZTS_{0.25}Se_{0.75}$ is stable.

Electronic Structure and Defect Energies in AgZTS-Se: It was speculated that if the metal exchange defect energy could be increased, the number of exchange sites creating band-edge states could be reduced thereby improving the Voc. While this is not the sole cause of the Voc deficit, it is more than 200 mV. A supercell of AgZTS-Se was relaxed using the same DFT technique and parameters as previously employed for CZTS-Se. As shown in Fig 39, the defect-free supercell with 75% Se and 25% S, has a band gap of 0.80 eV. Addition of the S-Se exchange sites does not induce any band edge state. However, the Ag-Zn exchange site causes a 0.2 eV decrease in band gap. As shown in Table 4, the defect formation energy for Cu-Zn in CZTS0.25Se0.75 and Ag-Zn in AgZTS0.25Se0.75 were calculated. The defect configurations were calculated: with 1 defect per supercell (12.5% of sites), with 2 defects per supercell (25% of the sites), and with 4 defects per supercell (50% of the sites). For both materials, as the defect density increases, there is a dramatic decrease in the energy of defect formation. This means that as one cools the material, if one can lower the defect density to 12.5%, it will be easier to remove the remaining defects. Most importantly, the Ag-Zn exchange defects in AgZTS0.25Se0.75 have around 2 times higher the formation energy in comparison with the Cu-Zn defects in CZTS0.25Se0.75, which would imply a 10x lower concentration at equilibrium. This has motivated experimental studies of this material.

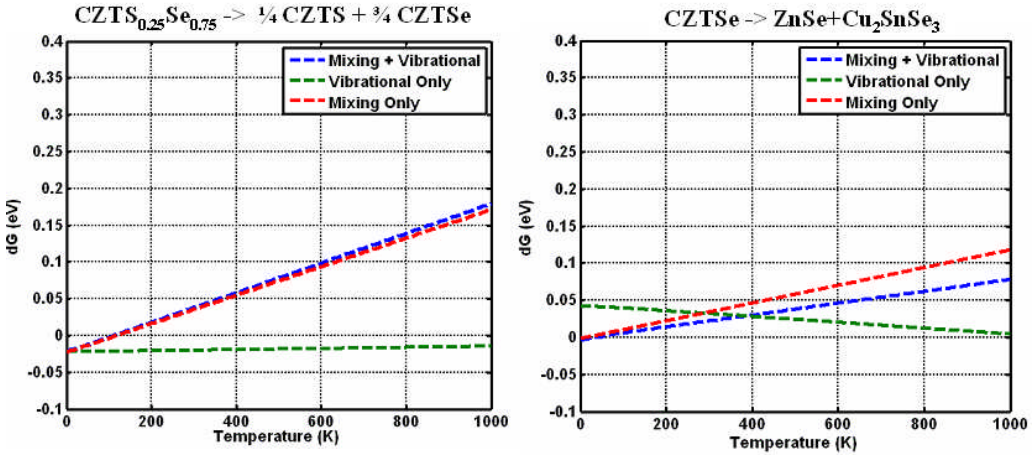

Figure 38. Thermal Stability (Change of Gibbs Energy) of $CZTS_{0.25}Se_{0.75}$ and CZTSe. The stability is shown for Gmix only, Gvib only, and Gmix + Gvib.

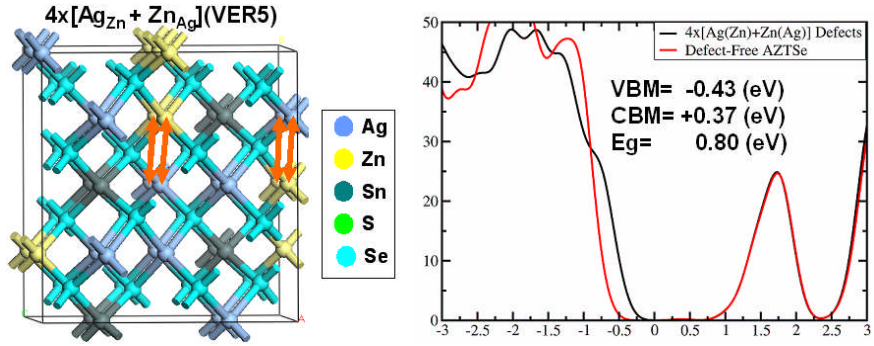

Figure 39. Bulk $AgZTS_{0.25}Se_{0.75}$ unit cell electronic structure calculated with HSE using same parameters as $CZTS_{0.25}Se_{0.75}$. After defects were inserted, supercell was relaxed at variable volume to remove strain. With 4 Ag-Zn exchange defects in 4 unit cells (complete Ag-Zn intermixing), there is a VB edge state.

The defect formation energies in AgZTSe and CZTS0.25Se0.75 were calculated as a function of defect density for 13 different defects. It was found that for all concentrations the defect formation energies for I-II exchange (i.e. Ag/Zn or Cu/Zn) are 1.6-3.8 times higher in AgZTSe than CZTS0.25Se0.75. This implies that the bulk defect concentration in AgZTSe should be 10x lower than in CZTS0.25Se0.75 and the defects in AgZTSe should more readily cluster (These results have now been published.). This is a key finding since it implies that AgZTSe has the potential to have the low bulk defect density of CIGS and the related high PV efficiency.

Defect cluster	Formation energy (eV)
$[Zn_{Ag}+Ag_{Zn}]$ (VER 1)	+0.46
2 $[Zn_{Ag}+Ag_{Zn}]$ (VER 1)	+0.79 (+0.395 eV/pair)
4 $[Zn_{Ag}+Ag_{Zn}]$ (VER 1)	+1.28 (+0.32 eV/pair)
$[Zn_{Cu}+Cu_{Zn}]$ (VER 1)	+0.22
2 $[Zn_{Cu}+Cu_{Zn}]$ (VER 1)	+0.45 (+0.225 eV/pair)
4 $[Zn_{Cu}+Cu_{Zn}]$ (VER 1)	+0.53 (+0.133 eV/pair)

Table 4. Formation energy of cation antisite pairs in $AZTS_{0.25}Se_{0.75}$ and $CZTS_{0.25}Se_{0.75}$, as a function of defect pair density per supercell.

Interfaces between a-MoOx and CZTS0.25Se0.75: We previously had found that the CZTS0.25Se0.75 surface is most stable when it is terminated by S and Se consistent with S and Se filled lone pair orbital (filled dangling bonds) being chemically stable. Several bilayers of a-MoOx were modeled including a full bilayer of a-MoO3, a full bilayer of a-MoO2, and a monolayer of a-MoO3/monolayer a-MoO2/CZTS0.25Se0.75. To form an electrically and chemically passive interface on the S/Se termination, we need to form Mo-S and Mo-Se bonds since they mimic the bulk bonds of CZTS0.25Se0.75. When a-MoO3

	Version	$CZTS_{0.25}Se_{0.75}$ (eV)	AZTSe (eV)	Ratio
[Zn(Cu)+Cu(Zn)] or [Ag(Zn)+Zn(Ag)]	1	+0.22	+0.80	3.6
	2	+0.18	+0.64	3.6
	3	+0.17	+0.63	3.7
2×[Zn(Cu)+Cu(Zn)] or 2×[Ag(Zn)+Zn(Ag)]	1	+0.45 (+0.225 eV/pair)	+1.20 (+0.600 eV/pair)	2.7
	2	+0.30 (+0.150 eV/pair)	+1.05 (+0.525 eV/pair)	3.5
	3	+0.43 (+0.215 eV/pair)	+1.03 (+0.515 eV/pair)	2.4
	4 (CL)	+0.26 (+0.130 eV/pair)	+0.86 (+0.430 eV/pair)	3.3
	5 (CL)	+0.25 (+0.125 eV/pair)	+0.95 (+0.475 eV/pair)	3.8
4×[Zn(Cu)+Cu(Zn)] or 4×[Ag(Zn)+Zn(Ag)]	1	+0.53 (+0.133 eV/pair)	+1.68 (+0.420 eV/pair)	3.2
	2	+0.58 (+0.145 eV/pair)	+0.93 (+0.233 eV/pair)	1.6
	3	+0.65 (+0.163 eV/pair)	+1.17 (+0.293 eV/pair)	1.8
	4 (CL)	+0.73 (+0.183 eV/pair)	+1.33 (+0.333 eV/pair)	1.8
	5 (CL)	+0.47 (+0.118 eV/pair)	+1.07 (+0.268 eV/pair)	2.3

Table 5. Defect formation energies in $CZTS_{0.25}Se_{0.75}$ and AZTSe systems. Ratio is a parameter defined as $E_{def}(AZTSe)/E_{def}(CZTS_{0.25}Se_{0.75})$.

directly bonds to CZTS-Se, the Mo atoms become over-coordinated so the interface is disordered. However when a-MoO2 bonds at the interface, the addition of the Mo-S and Mo-Se bonds restores the Mo to its preferred coordination and valence state so a near perfectly order interface is formed (Fig 40a); the interface is stable even with high temperature annealing (Fig 40b). The oxide second layer should be close to fully stoichiometric a-MoO3 to prevent disruption of the near perfect a-MoO2/CZTS0.25Se0.75 interface (Fig 40c). The a-MoO3/a-MoO2/CZTS0.25Se0.75 is stable with high temperature annealing preserving the Mo-S and Mo-Se interface. DFT calculations of the electronic structure of the a-MoO3/a-MoO2/CZTS0.25Se0.75 stack are consistent with charge transfer at the interface; the band gap states (Fig 40e) are not located at the interface but instead located on opposite sides of the interface (Fig 40f).

The strong polarity of Mo-S and and Mo-Se bonds is consistent with the interface charge separation.

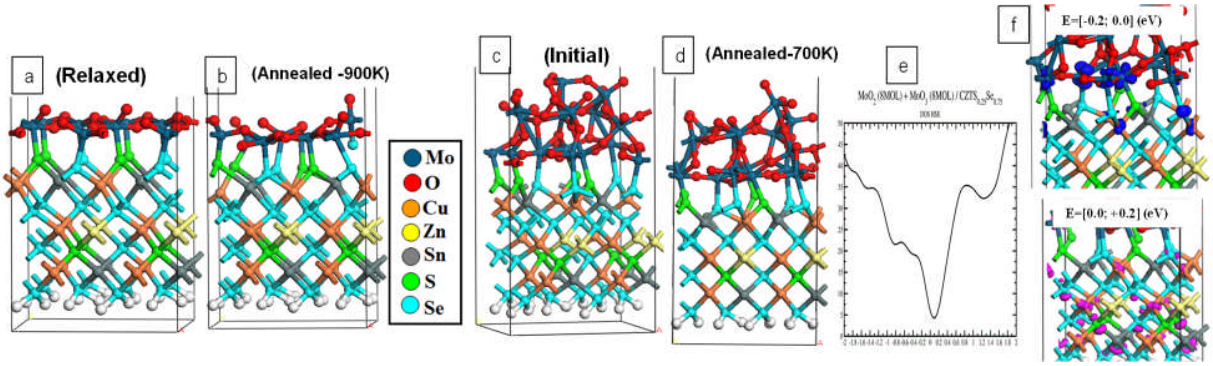

Figure 40**:** Density Functional Theory Molecular Dynamics (DFT-MD) Simulations of the a-MoOx/$CZTS_{0.25}Se_{0.75}$ Interface. (a) Initial a-MoO_2/CZTS-Se stack with S,Se termination and formation of Mo-S and Mo-Se bonds; (b) a-MoO_2/CZTS-Se stack after 900K anneal, cooling and relaxation showing preservation of the Mo-S and Mo-Se bonds and a near perfect 2D structured interface. (c) a-MoO_3/ a-MoO_2/CZTS-Se initial stack with S,Se termination and formation of Mo-S and Mo-Se bonds; (d) a-MoO_3/ a-MoO_2/CZTS-Se initial stack after 700K anneal, cooling and relaxation showing preservation of the Mo-S and Mo-Se bonds and a near perfect 2D structured interface. (e) DOS of the annealed a-MoO_3/a-MoO_2/CZTS-Se stack showing only a band minimum. (f) Band-decomposed charge density of the a-MoO_3/a-MoO_2/CZTS-Se stack showing the valence band stack (blue-top) in the oxide and conduction band states (pink-lower) in the CZTS-Se consistent with an absence of interface states and instead charge separation due to polar interface bonds.

Conclusions

There were a number of key results and significant progress in both understanding of the CZTS,Se material and its performance as a photovoltaic absorber. Given the intransigent nature of CZTS,Se owing to its possession of a high density of point and clusters of defects, new materials and engineered contacts were created. As they say necessity is the “mother-of-creation”! Herein is a summary of achievements both in the realm of scientific reporting and technical:

REPORTING

- >30 papers published in high impact journals (AEM, AM, J.Chem. Phys. APL, JAP, IEEE J. Photovolt. ACS Mat. MRS Bull. And Comm.)
- >55 conference presentations (MRS, PVSC, AVS, APS, ACS, SPIE)
- 14 Invited Talks, Keynotes, Plenary and Presidential Symposium
- >19 Patents filed
- 3 PhD’s conferred
- 2 grad student awards

TECHNICAL- Analysis and Understanding

- Bulk single crystal efficiency increased from ~1% at start ot ~10%- **World Best,** also achieved single crystals with sizes >2mm

- CZTSe efficiency of 11.6% achieved and record minority carrier mobility of 690 cm^2/V-sec- both **World Best**
- Voc deficit reduced from >600mV to 526 mV in exfoliated CZTS,Se device and 563 mV in single crystal
- First AZTSe device, efficiency 5.1% **World Best**
- $(Ag_{0.1}Cu_{0.9})$ZTSe 10.2% efficiency, 60 mV reduction in Voc deficit **World Best**
- **16.2%** efficiency <200K- highest kesterite efficiency at any temp
- Exfoliation experiments
    - 1µm solution deposited device with 10.4%
    - Demonstrated Voc increases of >50mV via high WF/reflective back contact
    - 11.4% efficiency with Voc 672 mV World Best
    - Series connect high S monolithic device (9 devices) Voc=5.7V, 20 mA current at 1 Sun, ~2V at 10-3 Suns, never before achieved

TECHNICAL- Analysis and Understanding

- DFT calculations
    - Gibbs mixing +vibrational contributions key to stabilizing stable CZTS,Se phase
    - Calculation of antisite defect formation energies that limit Voc and Ag derived barrier to formation leading to a 10X reduction of defect density, confirmed by PL studies
    - MoO_3/MoO_2 interface calcs showing role of oxidation in reducing defects
- Auger Nanoprobe and KPFM
    - Direct observation of SnOx at grain boundaries explains why air anneal passivates and why device performance increases
    - First nanoscale studies of elemental composition at grain boundaries, surfaces and interfaces
    - Development of grazing incidence cryo-FIB and electronics of buried interfaces
- Invention of New Hall Probe and Methodology
    - Table-top system using rotating rare earth magnets measures carrier densities in the absorber films,
    - Development of photohall measurements
    - Patented and commercialized this technology
- Femtosecond Ultraviolet Photoelectron Spectroscopy
    - Directly measured band bending at p-n junction and back contact junction
    - Straightforward measurement of Fermi level, valence and conduction band offsets in single measurement

These results point to an extremely productive effort to identify constraining issues, to rectify many problems, increase performance and to provide engineering solutions that make CZTS,Se a viable absorber for many applications.

Overall conclusions are that CZTS,Se remains a promising non-toxic earth abundant PV absorber material. Given the initial success of alloying small amounts of Ag into the kesterite lattice and owing to the >16% efficiency below 200K, indicates that bulk point defects can be mitigated to increase the room temperature efficiency of this material. Because of the large phase space of processing conditions when any change is made to

a material, such as adding small amounts of Ag that necessitates new annealing protocols, further work is required to optimize these conditions and achieve higher efficiencies. Furthermore additional optimizations are conceived of for the future. An example would be in the area of bifacial energy generation in exfoliated CZTS,Se where the back surface, now accessible can be covered with transparent contacts that would allow additional light into the device.

Budget and Schedule

The project period of performance included three annual budget periods from 9/30/13 to 10/31/16. The total budget was $5.6M with a cost share requirement of 20%. The full budget was consumed and the cost share requirement was exceeded. There were no schedule changes.

Path Forward

At present plans at IBM for moving forward consist of utilizing CZTS,Se in an exfoliated form with high work function and reflective back contacts, connected in series and coupled with battery to create an energy harvesting solution for the “Internet-of-Things” series of devices that will be able to function autonomously. Since CZTS,Se is a non-toxic, earth abundant material, such devices will be environmentally friendly.

Additional work by IEC at U Delaware as described above consists of further growth of single crystals and deposition of ultrathin layers of CIGSe to enhance Voc. Manuscripts still in process will be finished and submitted to peer reviewed journals. Continued work on overall improvement to CZTS,Se performance as relates to the PV+battery work will continue. The champion solar cell, made using Br passivation, from ampoule SY24E, had an efficiency of 10% with qV_{def} = 540 meV. This result suggests that the bulk single crystal state of the art has reached the level where more process optimization such as reducing CdS thickness can surpass thin film efficiency levels. This platform should be used to continue work with band gap widening and bulk property refinement, such as longer run times to further enlarge crystal size.

References

[1] P. J. Cousins, D. D. Smith, H.-C. Luan, J. Manning, T. D. Dennis, A. Waldhauer, K. E. Wilson, G. Harley, and W. P. Mulligan, “Generation 3: Improved performance at lower cost,” in *Photovoltaic Specialists Conference (PVSC), 2010 35th IEEE*, 2010, pp. 275–278.

[2] M. A. Green, K. Emery, Y. Hishikawa, W. Warta, and E. D. Dunlop, “Solar cell efficiency tables (version 48),” *Prog. photovoltaics Res. Appl.*, vol. 24, no. 7, pp. 905–913, 2016.

[3] C. Candelise, M. Winskel, and R. Gross, “Implications for CdTe and CIGS technologies production costs of indium and tellurium scarcity,” *Prog. Photovoltaics Res. Appl.*, vol. 20, no. 6, pp. 816–831, 2012.

[4] M. Saliba, T. Matsui, J.-Y. Seo, K. Domanski, J.-P. Correa-Baena, M. K. Nazeeruddin, S. M. Zakeeruddin, W. Tress, A. Abate, and A. Hagfeldtd, “Energy & Environmental Science.”

[5] H. Katagiri, K. Jimbo, W. S. Maw, K. Oishi, M. Yamazaki, H. Araki, and A.

Takeuchi, “Development of CZTS-based thin film solar cells,” *Thin Solid Films*, vol. 517, no. 7, pp. 2455–2460, 2009.

[6] H. Katagiri, “Cu 2 ZnSnS 4 thin film solar cells,” *Thin Solid Films*, vol. 480, pp. 426–432, 2005.

[7] W. Wang, M. T. Winkler, O. Gunawan, T. Gokmen, T. K. Todorov, Y. Zhu, and D. B. Mitzi, “Device characteristics of CZTSSe thin-film solar cells with 12.6% efficiency,” *Adv. Energy Mater.*, vol. 4, no. 7, pp. 1–5, 2014.

[8] Y. S. Lee, T. Gershon, T. K. Todorov, W. Wang, M. T. Winkler, M. Hopstaken, O. Gunawan, and J. Kim, “Atomic Layer Deposited Aluminum Oxide for Interface Passivation of Cu2ZnSn (S, Se) 4 Thin-Film Solar Cells,” *Adv. Energy Mater.*, 2016.

[9] T. Gershon, K. Sardashti, O. Gunawan, R. Mankad, S. Singh, Y. S. Lee, J. A. Ott, A. Kummel, and R. Haight, “Photovoltaic Device with over 5% Efficiency Based on an n-Type Ag2ZnSnSe4 Absorber,” *Adv. Energy Mater.*, 2016.

[10] A. Nagaoka, K. Yoshino, H. Taniguchi, T. Taniyama, and H. Miyake, “Growth of Cu2ZnSnS4 Single Crystal by Traveling Heater Method,” *Jpn. J. Appl. Phys.*, vol. 50, p. 128001, Nov. 2011.

[11] A. Nagaoka, K. Yoshino, H. Taniguchi, T. Taniyama, and H. Miyake, “Growth of Cu2ZnSnSe4 single crystals from Sn solutions,” *J. Cryst. Growth*, vol. 354, no. 1, pp. 147–151, Sep. 2012.

[12] M. Grossberg, J. Krustok, T. Raadik, M. Kauk-Kuusik, and J. Raudoja, “Photoluminescence study of disordering in the cation sublattice of Cu2ZnSnS4,” *Curr. Appl. Phys.*, vol. 14, no. 11, pp. 1424–1427, 2014.

[13] J. Krustok, H. Collan, M. Yakushev, and K. Hjelt, “The role of spatial potential fluctuations in the shape of the PL bands of multinary semiconductor compounds,” *Phys. Scripta.1*, vol. T79, pp. 179–182, 1999.

[14] E. Chagarov, K. Sardashti, A. C. Kummel, Y. S. Lee, R. Haight, and T. S. Gershon, “Ag2ZnSn(S,Se)4: A highly promising absorber for thin film photovoltaics.,” *J. Chem. Phys.*, vol. 144, no. 10, p. 104704, 2016.

[15] C. Persson, “Electronic and optical properties of Cu2ZnSnS4 and Cu 2ZnSnSe4,” *J. Appl. Phys.*, vol. 107, no. 5, p. 053710, 2010.

[16] K. F. Tai, T. Gershon, O. Gunawan, and C. H. A. Huan, “Examination of electronic structure differences between CIGSSe and CZTSSe by photoluminescence study,” *J. Appl. Phys.*, vol. 117, no. 23, 2015.

[17] Z. Yuan, S. Chen, H. Xiang, X. Gong, A. Walsh, J. Park, I. Repins, and S. Wei, “Engineering Solar Cell Absorbers by Exploring the Band Alignment and Defect Disparity: The Case of Cu-and Ag-Based Kesterite Compounds,” *Adv. Funct. Mater.*, vol. 25, no. 43, pp. 6733–6743, 2015.

[18] T. Gershon, Y. S. Lee, P. Antunez, R. Mankad, S. Singh, D. Bishop, O. Gunawan, M. Hopstaken, and R. Haight, “Photovoltaic Materials and Devices Based on the Alloyed Kesterite Absorber ($Ag_x Cu_{1-x})_2 ZnSnSe_4$,” *Adv. Energy Mater.*, p. n/a–n/a, 2016.

[19] T. Gokmen, O. Gunawan, T. K. Todorov, and D. B. Mitzi, “Band tailing and efficiency limitation in kesterite solar cells,” *Appl. Phys. Lett.*, vol. 103, no. 10, pp. 1–12, 2013.

[20] S. Siebentritt, G. Rey, A. Finger, D. Regesch, J. Sendler, T. P. Weiss, and T.

Bertram, “What is the bandgap of kesterite?,” *Sol. Energy Mater. Sol. Cells*, 2015.
[21] T. Todorov, T. Gershon, O. Gunawan, C. Sturdevant, and S. Guha, “Perovskite-kesterite monolithic tandem solar cells with high open-circuit voltage,” *Appl. Phys. Lett.*, vol. 105, no. 17, pp. 1–6, 2014.
[22] D. Cheyns, B. Kam, K. Vasseur, P. Heremans, and B. P. Rand, “Structure induced conductivity enhancement in metal-doped molybdenum oxide thin films,” *J. Appl. Phys.*, vol. 113, no. 4, p. 43109, 2013.
[23] T. Minemoto, Y. Hashimoto, T. Satoh, T. Negami, H. Takakura, and Y. Hamakawa, “Cu(In,Ga)Se[sub 2] solar cells with controlled conduction band offset of window/Cu(In,Ga)Se[sub 2] layers,” *J. Appl. Phys.*, vol. 89, no. 12, p. 8327, 2001.
[24] D. Lim and R. Haight, “In situ photovoltage measurements using femtosecond pump-probe photoelectron spectroscopy and its application to metal–HfO2–Si structures,” *J. Vac. Sci. Technol. A*, vol. 23, no. 6, pp. 1698–1705, 2005.
[25] R. Haight, A. Barkhouse, O. Gunawan, B. Shin, M. Copel, M. Hopstaken, and D. B. Mitzi, “Band alignment at the Cu2ZnSn(SxSe1-x)4/CdS interface,” *Appl. Phys. Lett.*, vol. 98, no. 25, p. No pp yet given, 2011.
[26] D. A. R. Barkhouse, R. Haight, N. Sakai, H. Hiroi, H. Sugimoto, and D. B. Mitzi, “Cd-free buffer layer materials on Cu 2ZnSn(S xSe 1-x) 4: Band alignments with ZnO, ZnS, and In 2S 3,” *Appl. Phys. Lett.*, vol. 100, no. 19, pp. 4–9, 2012.
[27] T. Gershon, T. Gokmen, O. Gunawan, R. Haight, S. Guha, and B. Shin, “Understanding the relationship between Cu2ZnSn(S,Se)4 material properties and device performance,” *MRS Commun.*, vol. 4, no. 04, pp. 159–170, 2014.
[28] L. Sun, R. Haight, P. Sinsermsuksakul, S. Bok Kim, H. H. Park, and R. G. Gordon, “Band alignment of SnS/Zn(O,S) heterojunctions in SnS thin film solar cells,” *Appl. Phys. Lett.*, vol. 103, no. 18, 2013.
[29] T. Gokmen, O. Gunawan, and D. B. Mitzi, “Minority carrier diffusion length extraction in Cu2ZnSn(Se,S)4 solar cells,” *J. Appl. Phys.*, vol. 114, no. 11, p. 114511, 2013.
[30] Y. Liu, Y. Sun, and A. Rockett, “A new simulation software of solar cells—wxAMPS,” *Sol. Energy Mater. Sol. Cells*, vol. 98, pp. 124–128, 2012.
[31] K. Sardashti, R. Haight, T. Gokmen, W. Wang, L. Y. Chang, D. B. Mitzi, and A. C. Kummel, “Impact of nanoscale elemental distribution in high-performance kesterite solar cells,” *Adv. Energy Mater.*, vol. 5, no. 10, pp. 1–9, 2015.
[32] Y. S. Lee, T. Gershon, O. Gunawan, T. K. Todorov, T. Gokmen, Y. Virgus, and S. Guha, “Cu<inf>2</inf>ZnSnSe<inf>4</inf> thin-film solar cells by thermal co-evaporation with 11.6% efficiency and improved minority carrier diffusion length,” *Adv. Energy Mater.*, vol. 5, no. 7, pp. 2–5, 2015.
[33] K. F. Tai, O. Gunawan, M. Kuwahara, S. Chen, S. G. Mhaisalkar, C. H. A. Huan, and D. B. Mitzi, “Fill Factor Losses in Cu2ZnSn (SxSe1− x) 4 Solar Cells: Insights from Physical and Electrical Characterization of Devices and Exfoliated Films,” *Adv. Energy Mater.*, vol. 6, no. 3, 2016.
[34] O. Gunawan, Y. Virgus, and K. F. Tai, “A parallel dipole line system,” *Appl. Phys. Lett.*, vol. 106, no. 6, p. 62407, 2015.